Ground truth validated 3D electrical resistivity imaging of the archaeological deposits at Arma Veirana cave (northern Italy)

Published Version:
Torrese P., Zucca F., Martini S., Benazzi S., Drohobytsky D., Gravel-Miguel C., et al. (2022). Ground truth validated 3D electrical resistivity imaging of the archaeological deposits at Arma Veirana cave (northern Italy). JOURNAL OF QUATERNARY SCIENCE, 37(6), 1112-1132 [10.1002/jqs.3406].

Availability:
This version is available at: https://hdl.handle.net/11585/897304 since: 2024-01-18

Published:
DOI: http://doi.org/10.1002/jqs.3406

GROUND TRUTH VALIDATED 3D ELECTRICAL RESISTIVITY IMAGING OF THE ARCHAEOLOGICAL DEPOSITS AT ARMA VEIRANA CAVE (NORTHERN ITALY)

Torrese P.[1*], Zucca F.[1], Martini S.[2], Benazzi S. [3,4], Drohobytsky D. [5], Gravel-Miguel C.[6,7], Hodgkins J. [8], Meyer D. [5], Miller C. [9,10], Peresani M. [11,12], Orr C. [8], Riel-Salvatore J. [7], Strait D.S. [13,14], Negrino F. [15]

[1] Dipartimento di Scienze della Terra e dell'Ambiente, Università di Pavia, Pavia, Italy

[2] GEA Servizi di Geoarcheologia Srls, Mornico Losana, Pavia, Italy

[3] Dipartimento di Beni Culturali, Università di Bologna, Ravenna, Italy

[4] Department of Human Evolution, Max Planck Institute for Evolutionary Anthropology, Leipzig, Germany

[5] Cultural Heritage Engineering Initiative (CHEI), University of California San Diego, La Jolla, CA, USA

[6] School of Human Evolution and Social Change, Institute of Human Origins, Arizona State University, Tempe, AZ, USA

[7] Département d'Anthropologie, Université de Montréal, Montréal, QC, Canada

[8] Department of Anthropology, University of Colorado, Denver, CO, USA

[9] Institute for Archaeological Sciences and Senckenberg Centre for Human Evolution and Paleoenvironment, University of Tübingen, Tübingen, Germany

[10] SFF Centre for Early Sapiens Behaviour (SapienCE), University of Bergen, Bergen, Norway

[11] Dipartimento di Studi Umanistici, Sezione di Scienze Preistoriche e Antropologiche, Università di Ferrara, Ferrara, Italy

[12] Istituto di Geologia Ambientale e Geoingegneria, Consiglio Nazionale delle Ricerche, Milano, Italy

[13] Department of Anthropology, Washington University in St. Louis, St. Louis, MO, USA

[14] Palaeo-Research Institute, University of Johannesburg, Auckland Park, Gauteng, South Africa

[15] Dipartimento di Antichità, Filosofia, Storia (DAFIST), Università di Genova, Genova, Italy

*Corresponding author: patrizio.torrese@unipv.it

Abstract

We present 3D Electrical Resistivity Tomography (ERT) imaging of the archaeological deposits at Arma Veirana cave (Northern Italy), to date only partially explored. The archaeological importance of the cave is due to the presence of a rich Mousterian layer, traces of Late Upper Palaeolithic (Epigravettian) temporary occupations and an Early Mesolithic burial of a female newborn. ERT is rarely employed in Paleolithic cave contexts because Paleolithic remains are typically disseminated in loose deposits and either do not possess high electrical resistivity contrasts or are too small to be detected. Furthermore, some issues can derive from the confined environment

in caves. In this view, our study represents an opportunity to assess the capability of this geophysical method to retrieve subsurface information of Paleolithic cave deposits and create a framework for the improvement of ERT applications in such a peculiar cave context. The aim of this study was to define the features of the deposits (i.e., geometry, thickness, and sediment distribution) and to map the morphology of the underlying bedrock. Results reveal that the thickness of the deposits varies both along the primary axis of the cave and transverse to it. This study allowed the recognition of shallow, meter-sized, fine-grained sediment-filled structures with a longitudinal orientation with respect to the primary axis of the cave, as well as a possible erosional-like structure. The cross-validation of geophysical results with the archaeological evidence (the Early Mesolithic newborn burial and Epigravettian artefacts) confirms that the low-resistivity unit could be the most promising from an archaeological point of view.

Keywords: cave deposit, Pleistocene, Early Holocene, ERT, 3D resistivity imaging, geophysical investigations

1. INTRODUCTION

In general, one of the primary goals of a new archaeological excavation project is to document the formation of the site, as well as the extent of its deposit. At the Arma Veirana cave, which is the topic of the present study, only a small portion of the deposit has been explored during the four recent archaeological field seasons (Hodgkins et al., in review; Negrino et al., 2018). While recent documentations of exposed sections have provided a fair amount of data on some of the depositional history at the front of the cave, at present the depth and richness of the sediment remained unknown for all portions of the cave. Given the destructive nature of archaeological excavations, non-destructive in-depth investigation of the deposits is a valuable approach to help design future excavations. Specifically, at this point in the project, it became important to assess the extent and define the properties and volumes of potential artefact-bearing deposits before proceeding with further excavation.

In this context, the team turned to near-surface geophysical methods as an important tool to derive key information about underground properties and structures. Geophysical methods are an important component of geoarchaeological investigations. They allow non-invasive and rapid imaging of archaeological settings and help answer scientific questions by considering a site integrally within its geological surroundings. They are particularly useful in geoarchaeological investigations to define site stratigraphy, map site disturbance, and reconstruct palaeolandscapes (Sarris et al., 2018). However, geophysical techniques are seldom used to investigate Paleolithic archaeological sites (Obradovic et al., 2015; Abu Zeid et al., 2019), mostly due to those sites' sedimentary nature and the almost complete absence of architectural remains that can result in clear geophysical anomalies. The presence of numerous, thin, and closely packed occupation layers containing archaeological remains that are generally very small and would be destroyed by invasive investigations makes the contribution of geophysical methods significant (c.f. Abu Zeid et al., 2019). Schmidt et al. (2015) provide an overview of the issues to be considered when undertaking or commissioning geophysical survey in archaeology.

One of the most frequently used geophysical techniques is Electrical Resistivity Tomography (ERT). It is a quick and cost-effective method that provides a reliable imaging of the subsurface electrical resistivity pattern and allows identification of underground structures. ERT theory (cf., Dahlin and Loke, 1998; Loke et al., 2003) and application (cf. Griffiths and Barker, 1993; Guérin and Benderitter, 1995; Torrese, 2020; Torrese et al., 2021a) are well documented in geophysical research literature.

ERT is widely used in archaeological studies (Campana and Piro, 2008; Witten, 2017; El-Qady et al., 2019). It has been used to investigate site stratigraphy (Papadopoulos et al., 2006) and the sedimentological architecture (Yogeshwar et al., 2019), to detect changes in lithology and geology (Laigre et al. 2012; Scapozza and Laigre 2014), depositional targets and buried structures (Cozzolino et al., 2020; Papadopoulos et al., 2007; Supriyadi et al., 2019; Tsokas et al., 2009), to map remnants of past human occupation (Berge and Drahor, 2011a, 20011b; Matias et al., 2006; Papadopoulos et al., 2010; Thacker et al., 2002; Tsokas et al., 2018), to reconstruct palaeolandscapes (Papadopoulos et al., 2014) as well as to detect of offshore archaeological features (Sarris et al., 2014; Tonkov, 2014; Simyrdanis et al., 2015). ERT is also widely used to choose the most promising areas to excavate (Piroddi et al., 2020).

Paleolithic caves in temperate regions of Europe are often filled with deposits that are poorly sorted and display a wide range of grain-sizes, from large blocks of roof fall (éboulis) to silt and clays (Goldberg and Sherwood, 2006; Mallol and Goldberg, 2017). Differently from other archaeological settings with localized and large sized anomalies easily detectable by ERT, the Paleolithic remains contained in such loose deposits are disseminated and either do not possess high electrical resistivity contrasts or are too small to be detected. This explains why ERT is rarely employed in Paleolithic cave contexts. Furthermore, given that the depth of investigation provided by ERT is tied to the length of the electrode array deployed, some issues can derive from the confined environment in caves (c.f. Abu Zeid et al., 2019).

Previous geophysical studies performed in Paleolithic caves focused mainly on retrieving the cave geometry and investigating the presence of voids (Beck and Weinstein-Evron, 1997; Jol et al., 2002; Quarto et al.,2007; Shopov et al., 2008). To our knowledge, ERT-based studies meant to document the features of the deposits and map the morphology of the underlying bedrock of Paleolithic caves are so far limited (Abu Zeid et al., 2019).

In this view, our ERT based study of the archaeological deposits at Arma Veirana cave represents an opportunity to assess the capability of this geophysical method to retrieve subsurface information of Paleolithic cave deposits and create a framework to improve ERT applications in such a peculiar context. As primary goals, the study aimed to create a three dimensional (3D) resistivity model of the archaeological deposits at Arma Veirana cave, to identify the volume of the deposits (or sediments, defined as detrital, loose, explorable materials, i.e., grains of clay, silt, sand and gravel) with the highest archaeological potential in terms of geometry, thickness and sediment distribution, and to map the morphology of the bedrock. This work leads to methodological insights about how to improve both efficiency and effectiveness of future archaeological campaigns inside caves, especially suitable for the Palaeolithic age. New insights on the development of Arma Veirana cave and on the nature of its sedimentary infill are also provided, thereby enabling a better understanding of the depositional processes involved in the formation of this important archaeological site. This information will be useful in the planning of long-term field-investigations and to locate areas that should be the focus of future excavations.

1.1. The ERT technique and the resistivity signature of the target

Electrical Resistivity Tomography (ERT) is based on a multi-electrode system applying direct current into the ground by means of two current electrodes and measures the resulting voltage via two potential electrodes; each of the electrodes alternatively acts as a current and potential electrode. To obtain a true resistivity model of the subsurface, an inversion procedure is needed (Loke and Barker, 1996). The arrangement of current and potential electrodes during the measurement is dependent on the chosen electrode array. The most frequently used arrays are the dipole–dipole, the Wenner, and the Wenner-Schlumberger arrays (e.g., Kneisel, 2006; Schrott and Sass, 2008). The dipole–dipole array uses two current electrodes on one side and two potential electrodes on the other side. This method is especially suitable for the detection of vertical structures, as it shows high lateral resolution, but it is too sensitive to near-surface anomalies (Szalai and Szarka, 2008a). The Wenner array comprises four equally spaced electrodes deployed in a line in which potential electrodes are located between current electrodes. The method is especially suitable for the detection of horizontal structures as it shows high vertical resolution, but it has shallower penetration and less subsurface information than the dipole–dipole array (Szalai et al., 2009). The Wenner-Schlumberger array is similar to the Wenner array; potential electrode spacing is constant but current electrode spacing is logarithmically increased. This array is especially appropriate for the detection of horizontal structures since it shows high vertical resolution like the Wenner array, but it has shallower penetration and less subsurface information than the dipole–dipole array. As each array has different disadvantages, we combined all of them here to get beyond their individual limits and obtain more accurate models.

ERT allows the characterization of subsurface materials based on their electrical properties. Changes in electrical resistivity correlate with variation in solid material (minerals and rocks), water saturation, fluid conductivity and porosity, which may be used to map stratigraphic units, geological structure, fractures, groundwater, and anthropogenic structures. ERT has been successfully used to identify and map low-resistivity volumes such as fine-grained archaeological deposits (Abu Zeid et al., 2019; Becker et al., 2019), as well as typically high resistivity structures, including bedrock, wall pipes, roads (Tsokas et al., 2009), foundations (Drahor et al., 2008), ditches, palaeochannels, internal structures in mounds and barrows (Astin et al., 2007; Papadopoulos et al., 2020), buried chambers and cavities (Cardarelli et al., 2006; Deiana et al., 2018), caves, karst features, sinkholes, and cavities (e.g., Al-Zoubi et al., 2007; Carrière et al., 2013; Maillol et al., 1999; Rainone et al. 2015; Satitpittakul et al., 2013; Smith, 1986; Torrese, 2020; Torrese et al., 2021a; Van Schoor, 2002; Zhu et al., 2011), offshore archaeological features (Sarris et al. 2014; Tonkov 2014; Simyrdanis et al. 2015).

One of the most important targets of ERT application in archaeological studies is the depth to the bedrock. Accurate information about bedrock’s morphology and depth can vastly improve excavation planning. Bedrock and sediments have typically different electrical resistivity; therefore, the bedrock’s buried surface can be measured as a high-contrast boundary in an electrical resistivity model. In the case of irregular morphology of bedrock, 3D ERT is required to build a more complete and accurate model of it.

The resistivity signature of the target depends on its size in relation to its depth and on the contrast between its resistivity and that of the surrounding (host) rock. The amplitude of resistivity anomalies is an inverse function of the distance between the measurement points and the cavity. The depth of investigation and the vertical and horizontal resolutions of ERT surveys are linked to: i) the electrode spacing, ii) the configuration array, iii) the quadrupole sequence, iv) the signal-to-noise ratio (SNR), v) the contrast between the resistivity of the target, and vi) the surrounding rock and/or background resistivity.

The ERT method has been applied at Arma Veirana cave because it is particularly effective in such a geological setting (i.e., where the target deposits consist mainly of fine deposits bounded below and laterally by limestone rocks). In this context, we expected ERT to provide an accurate model of the archaeological deposits' depth and position thanks to their low resistivity while the hosting rocks are of high resistivity.

1.2. ERT application inside caves

Applying ERT inside caves (Abu-Zeid et al., 2019; Hancock, 1999; Olenchenko et al., 2019; Osipova et al., 2020; Pringle et al., 2002) entails several issues caused by limited space for measurements and the complexity of the surrounding medium's structure as compared to above-ground measurements. Olenchenko et al. (2020) performed numerical experiments to assess the effect of the 3D cave geometry on the results of an ERT inversion. They found that variations of cave geometry parameters result in unexpected false anomalies, and that considerable errors in bedrock location and resistivity can occur. The authors suggested that two-dimensional (2D) ERT generally cannot be applied inside a cave whose half-width is smaller than the thickness of sediments; 3D surveys do not essentially improve the quality of results.

Findings from Olenchenko et al. (2020) on the use of ERT inside caves are consistent with results obtained by Fikos et al. (2019) who evaluated the ability of 2D ERT to provide effective results along profiles undertaken close and parallel to the vertical cave walls. By combining numerical modelling with field data, the authors found that if the distance between ERT profiles and the cave walls becomes too small, the high resistivity of the cave walls masks the conductive sediment layer. Furthermore, the resistivity of the sediments is significantly overestimated thus posing possible problems in the interpretation process.

However, as suggested by Olenchenko et al. (2020), in the case of downward diverging cave walls, as occurs at Arma Veirana cave (Fig. 1), an accurate resistivity model can be obtained. In such a case, despite being within a 3D cave geometry, the electric current is distributed approximately as in 2D medium. Therefore, ERT in caves with similar geometry can yield reliable results on the morphology of bedrock surface, the thickness of sedimentary layers, and size and position of inclusions such as fallen fragments of roof therein. Under these conditions, 3D surveys improve the quality of results, thus providing more complete and accurate models than 2D surveys.

2. ARMA VEIRANA

Arma Veirana, also known as Arma della Costa di Cerisola (Dal Bo et al., 1978), is located in the municipality of Erli, in the Savona province (Liguria, Northern Italy). It is situated in calcareous rocks of the Castelvecchio-Cerisola Unit of the Ligurian Briançonnais domain (Decarlis & Lualdi, 2009) and consists of a SE/NW-orientated chamber 44 meters long with an upslope of 4 meters between the cave entrance and its termination (Fig. 1).

The archaeological importance of the cave was first recognized in 2006 by Giuseppe Vicino, curator of the Museo Archeologico del Finale (Savona), who collected Middle and Upper Palaeolithic artefacts from the removed deposit. Formal excavations begun in 2015 and lasted until 2018.

To date, the main objective of the archaeological fieldwork was to document the cave's stratigraphy, which was initially visible in pits exposed by looters. Excavations at Arma Veirana have focused on several locations within the cave, exposing stratigraphic sections that span several lithological units referred to as stratigraphic aggregates (StratAggs) in our excavation system (equivalent to what are often called "layers"). The excavations exposed a rich Mousterian layer at the bottom of the main trench (stratigraphic section a-b, Fig. 2), which is located near the entrance of the cave, and traces of Late Upper Palaeolithic (Epigravettian) occupations in the upper aggregates. As reported in Hodgkins et al. (in review), an Early Mesolithic burial (10.280-9.924 cal BP) of a 40-50 days-old female newborn (AVH-1, nicknamed "Neve") was recovered in 2017 within an approximately 15 cm deep oval pit (< 600 cm^2 in area) cut into underlying late Epigravettian deposits. The burial feature containing the newborn remains was exposed after removing a thin layer of surficial deposits and appears to be intrusive into the underlying stratigraphic aggregate "Yellow Silt" (YS).

Numerous radiocarbon dates have been obtained, DNA samples collected, and traces of cryptotephra identified in correspondence of the Middle Paleolithic layers (Hirniak et al., 2020). The analysis of the archaeological finds and other geoarchaeological evidence is underway.

3. GEOLOGICAL AND ARCHAEOLOGICAL SETTING OF THE CAVE

3.1. Geological setting

The entrance of the Arma Veirana cave is located in a tight antiform syncline (Goudie, 2004) (interlimb angle > 30°) at the stratigraphic contact (Dallagiovanna et al., 2011) between the Val Tanarello limestone of the Kimmeridgian– Berriasian age (Bertok et al., 2011) at the top and the calcareous schists and shales of the Caprauna Formation of late Cretaceous-middle Paleogene period (Dallagiovanna et al., 2011) at the bottom (Fig. S2 in the Supporting Information); it is an uncommon case of an inner-fold cave, where the access opening corresponds to a rock fall related to the Rio Neva valley evolution (Fig 1d).

With regard to the cave genesis and evolution, we identify here the model that best fits with field observations and the results of the geophysical investigation. In short terms, even if carbonate dissolution may have had some role in the first stage of its development (Dubois et al., 2011; Quinif, 2014; 2018), Arma Veirana is not an epigenetic solution cave. According to the most recent classification (Oberender and Plan, 2018) it is a "pseudo-endokarst" produced first by "mechanical weathering" (first order type cave genesis according to Quinif and Bruxelles, 2011) followed by alterite removing through "piping" (second order cave genesis) with the final development of a "suffusion cave" (Sauro, 2005; Sola et al., 2007).

Speleogenesis models of the Veirana cave, its relationships with the paleo-evolution of the Rio Neva paleovalley, the development of the other caves and canyons of the area and their relations with prehistoric anthropic settlement are active areas of research.

3.2. Archaeological evidence

To document the history of the cave, several archaeological pits have been excavated in different parts of the cave, with the deepest trench dug near the entrance of the cave. This main trench is about 1.2 m deep but has not yet reached the bedrock. Yet, the sediments exposed by this trench have revealed interesting anthropic evidence pertaining to the Middle Palaeolithic. The stratigraphy of this trench consists of five distinct stratigraphic aggregates (or layers) named, from top to bottom: "Disturbed" (D), "Rocky Brown" (RB), "Consolidated Strong Brown" (CSB), "Granular" (Gr) and "Black Mousterian" (BM) (Figs. 3 and S1 in the Supporting Information) that are differentiated from each other through variation in grain size, color, fabric, and structures. Radiocarbon dates obtained on material from those aggregates show that they are older than 50 ky BP.

Anthropic evidence is mainly concentrated in the layer at the base of the currently exposed stratigraphy, the BM aggregate, a 20-30 cm thick silty-sand layer with medium to small gravel with a dark greyish brown colour, due to the presence of manganese oxide staining but also numerous, silt and sand-sized fragments of combustion residues (e.g., charcoal). This aggregate has provided abundant fauna, which is often fragmented and bears anthropogenic cut marks, along with numerous Mousterian lithic artefacts (Middle Palaeolithic).

The aggregates above BM have lower artefact density, suggesting that the cave was not occupied as intensely during the accumulation of the deposit. The Gr is a narrow aggregate characterised by medium sandy silt with granules and gravel, with color varying around 10YR 4/4 to 10YR 4/3 (brown to dark yellowish brown). It exhibits a coarse crumb structure. It has a relatively high proportion of éboulis, which is mostly dominated by sub-angular to sub-rounded clasts that appear weathered and are on average 5-10cm in size. The proportion of éboulis decreases to the east, however, where éboulis is rarer. Portions of Gr appear cemented by secondary carbonate, forming a weak breccia.

Above Gr, the CSB is a clayey silt with fine sand and gravel. It appears more compact than Gr and displays a massive structure. The color is dark yellowish brown (10YR 4/4). Larger blocks of éboulis are relatively rare and consist mostly of 5cm-sized sub-angular to angular clasts which are locally organized into horizontally oriented lenses.

The RB sits on top of the CSB. RB is a clayey silt with fine sand and gravel and displays a weakly developed subangular blocks structure; the color is dark yellowish brown (10YR 4/4). RB contains a relatively high proportion of subangular to angular blocks of éboulis which are generally 10-15cm in size. These occur in higher proportion than in CSB.

An erosional unconformity distinguishes RB from the overlying D aggregate. D is a clayey silt with minor sand and gravel components with a dark greyish brown color. It appears to be modern surficial deposits, which are expressed either as sedimentary infillings within the rill system or as alteration surfaces formed directly on RB.

Higher in the cave deposits, (south of the main excavation trench), the YS aggregate is a 20 cm thick layer containing Late Upper Palaeolithic artefacts (Epigravettian). YS appears to be a clayey silt with minor sand and gravel components. Larger blocks of éboulis are rare, and most are between 5-7cm in size. They appear subrounded and display no preferred orientation. The color of YS is similar to RB (10YR 4/4) although it locally appears more yellowish in color. The Early Mesolithic burial was found inside a pit dug into the YS, ~2 m from the east wall of the cave (excavation square 2N1E in Fig. 2) (Hodgkins et al., in review). YS was readily distinguishable from the burial pit which was darker in color and had a high proportion of coarse material, including charcoal and bone.

The aforementioned erosional unconformity crosscuts several of the aggregates, so that towards the entrance of the cave D unconformably covers RB, whereas it covers YS towards the back and near the burial (Fig. 3). It is currently unknown whether the unconformity is local or cave-wide. Fig. S1 in the Supporting Information provides detailed images of the aggregates.

Dates of stratigraphic aggregates reported in this paper derive from ^{14}C Accelerator Mass Spectrometry (AMS) dating of faunal bone. Calibrations were done using IntCal20 (Reimer et al., 2020) in the OxCal 4.4 program (Ramsey, 2009).

4 MATERIALS AND METHODS

4.1. Data collection

3D ERT data were collected on June 27th 2018 with a fully automatic multi-electrode resistivity meter SYSCAL Jr Switch-48 by IRIS Instruments. A surface snake grid comprised of 8 x 6 electrodes spaced ~1.5 m apart both along the X and Y axes was used (Fig. 2). The electrodes could not be placed in a perfectly regular grid due to the presence of blocks, boulders, and calcite concretions on the ground (Figs. 4a-c). Despite this, the grid created allowed analysing an area of 10.5 m x 7.5 m with a maximum depth of ~ 2 m.

Data were collected using different electrode arrays: 202 dipole-dipole (DD) measures, 96 Wenner (W) measures, 134 Wenner-Schlumberger (WS) measures, 328 Pseudo Pole-Dipole measures (PsPD), for a total of 760 quadrupole measures for the whole model. The Pseudo Pole-Dipole array was comprised of two remote electrodes (one for forward and the other for reverse measurements, aligned along the axis of the cave) placed 25 m away from the centre of the grid (Fig. 4d). Because it uses a remote electrode with a finite distance location instead of a remote electrode with an infinite distance location provided for by theoretical Pole–Dipole (Razafindratsima and Lataste, 2014; Robain et al., 1999), this array has been named Pseudo Pole–Dipole rather than Pole-Dipole. Only forward measurements (no reverse measurements) were simulated with the PsPD array.

The data obtained with these arrays differed in resolution. Following Szalai et al. (2009), they were merged to deliver better detectability and imaging and, therefore, provide more accurate inverse models.

Details on raw data quality are provided in Table S1 in the Supporting Information.

4.2. Data inversion

No data processing (pre-inversion) was required to remove outliers from apparent (raw) resistivity data. The dataset, indeed, does not present any problematic data such as, for example, unrealistically high resistivity (>10000 Ω·m) or too-high standard deviation (>10 Ω·m).

Then, ERTLab Solver (by Multi-Phase Technologies LLC, Geostudi Astier srl) based on tetrahedral Finite Element Modelling (FEM) was used for data inversion. Tetrahedral discretization was used in both forward and inverse modelling. The foreground region was discretized using a ≈ 0.74 m element size along the X and Y, i.e., half the average electrode spacing and a ≈ 0.07 m element size along the Z direction to give the model higher accuracy. This created a 3D resistivity grid, 11 m x 8 m x ≈ 2 m in size. The background region was discretized using an increasing element size towards the outside of the domain, according to the sequence: 1×, 1×, 2×, 4× and 8× the foreground element size.

The forward modelling was performed using mixed boundary conditions (Dirichlet-Neumann) and a tolerance (stop criterion) of 1.0E-7 for a Symmetric Successive Over-Relaxation Conjugate Gradient (SSORCG) iterative solver. Data inversion was based on a least-squares smoothness constrained approach (LaBrecque et al., 1996). Noise was appropriately managed using a data-weighting algorithm (Morelli and LaBrecque, 1996) that allows the adaptive changes of the variance matrix after each iteration for those data points that are poorly fitted by the model. The inverse modelling was performed using a maximum number of internal inverse Preconditioned Conjugate Gradient (PCG) iterations of 5 and a tolerance (stop criterion) for inverse PCG iterations of 0.001. The amount of roughness from one iteration to the next was controlled to assess maximum layering: a low value of reweight constant (0.1) was set with the objective of generating maximum heterogeneity.

The inverse resistivity models (i.e., models with true resistivity rather than apparent or raw resistivity) were obtained by inverting the datasets acquired through single arrays, or by merging and jointly inverting datasets from different arrays which can deliver better detectability and imaging and, hence, provide more accurate inverse models (Szalai et al., 2009; Torrese, 2020) and more reliable ERT imaging (de la Vega et al., 2003; Seaton and Burbey, 2002). Inversion involved the application of homogeneous starting models that set the average measured apparent resistivity value at each node. The final inverse resistivity models were chosen based on the minimum data residual (or misfit error).

Details on the misfit of inverted data are provided in Table S2 in the Supporting Information.

4.3. Bulk total porosity estimation

A realistic, albeit presumed and rough (in the absence of specific measurements), estimate of the bulk total porosity ∅ for the different resistivity units revealed by ERT was obtained by applying the empirical relationship proposed by Archie (1942)

$$C_t = \frac{1}{a} C_w \emptyset^m S_w^n \quad (1)$$

where C_t is the electrical conductivity of the fluid impregnated deposit/rock, a is the tortuosity factor, C_w is the electrical conductivity of the fluid impregnating the deposit/rock, ∅ is the total porosity of the deposit/rock, m is the cementation exponent of the deposit/rock, S_w is the fluid saturation, and n is the saturation exponent.

The tortuosity factor a, dimensionless, is related to the path length of the current flow and is used to correct for variation in compaction, pore structure and grain size. Its value typically ranges between 0.5 and 1.5. The cementation exponent m, dimensionless, indicates reduction in the number and size of pore openings. It is affected by lithology, porosity, degrees of compaction and cementation, and age. Its value typically ranges between 1.3 and 2.35 (Salem and Chilingarian, 1999). These factors can be obtained from core analysis. Log–log plot of total porosity ∅ versus formation factor (Archie, 1942) is used to determine a and m: the tortuosity factor a is the intercept of the least square fit straight line of the plotted points where $\emptyset = 1$, while the cementation exponent m is determined from the negative slope of the line (Rezaee et al., 2007).

Archie's law relates the in-situ electrical conductivity of a porous rock to its total porosity and water saturation. It is a purely empirical law attempting to describe ion flow in clay-free porous rocks, with varying intergranular porosity. Electrical conduction is assumed not to be present within the rock grains or in fluids other than water.

5. RESULTS

5.1. Resistivity units

The inverse resistivity results are provided as 3D block models and plane slices extracted from the block models. All models shown here represent merged data obtained from dipole-dipole (DD), Wenner (W) and Wenner-Schlumberger (WS) arrays which delivered better detectability and imaging than single arrays only and, therefore, provided more accurate inverse models. Data acquired with Pseudo Pole-Dipole arrays were excluded from data merging because the difference in elevation between the remote electrodes installed inside and outside the cave affected their results and therefore, they did not provide any imaging improvements.

Misfit in terms of chi-squared errors (330 chi-squared error, 2.6 ohm·m Root Mean Square (RMR) error for the final iteration, Table S2 in the Supporting Information) suggests that inverse models are free of artifacts due to an inversion over-fit or excessive smoothing due to an inversion under-fit.

ERT models revealed that resistivity data could be separated into four resistivity units defined on the expected resistivity values for different lithological units (Figs. 5, 6): 1) the low-resistivity unit (L) ranging from 30 to 150 Ω·m is associated with fine-grained deposits (silty-sand); 2) the middle-low resistivity unit (ML) ranging from 150 to 300 Ω·m is related to fine to coarse-grained deposits (silty-sand with gravel and sporadic blocks); 3) the middle-high resistivity unit (MH) ranging from 300 to 440 Ω·m is associated with coarse-grained deposits (gravel and blocks in silty-sandy matrix) and heavily cracked/karst bedrock; 4) the high resistivity unit (H) ranging from 440 to 2.000 Ω·m is related to bedrock/boulders/breccia (limestone)/calcite concretions. The measured resistivity values suggest that the geological bodies corresponding to the resistivity units have a low clay content. Only the lowest resistivity deposits (approximately <100 Ω·m) included in the low-resistivity unit (30-150 Ω·m) have some clay content.

The spatial distribution of the different resistivity units related to detrital (loose) deposits shows a longitudinal orientation that follows the primary axis of the cave. The thickness of the archaeological deposits (different types of unconsolidated deposits, such as silty-sand with gravel and sporadic blocks) is highly variable along the primary axis of the cave and ranges between more than 1.5 meters at the entrance of the cave to less than 10 centimetres in the innermost part of the cave where it is discontinuous (Figs. 6-9). Fine-grained deposits (silty-sand) show greater consistency towards the entrance of the cave where they reach a maximum thickness of about 1 meter, in the northeast (Figs. 6, 7).

Transverse to the primary axis of the cave, the bedrock is relatively close to the surface at the southwest and deepens towards the northeast. Obviously, this change affects both volume and geometry of the overlying archaeological deposits which follows a gentler slope (Figs. 6-9).

The geometry, thickness, and distribution features of the different resistivity units revealed by plan (Fig. 5) and perspective views (Figs. 6-8) are also evident on the cross-section view (Fig. 9). The latter shows X-Y plane slices (x, y in Fig. 2) extracted from the 3D block model. The analysis of the cross-sections (Fig. 9) shows that the thickness of the archaeological deposits increases longitudinally towards the entrance of the cave and transversally towards the northeast.

From an archaeological point of view, the low-resistivity unit (30-150 Ω·m) associated with fine-grained deposits (silty-sand), is the most promising unit; i.e., this unit could represent the target deposits. This hypothesis is based on considerations inherent to the electrical resistivity found for this unit, which indicate the presence of fine-grained deposits that should be easy to excavate.

5.2. Bulk total porosity

The estimated bulk total porosity value $\emptyset$ ranges between 0.44 and 0.16 for the L unit, 0.16 and 0.13 for the ML unit, 0.13 and 0.1 for the MH unit and is equal to 0.1 for the H unit (Table 1). This estimation, which was based on the application of equation (1), involved:

C_t ranging between 3.3333e-2 S/m and 6.6667e-3 S/m for the L unit, ranging between 6.6667e-3 S/m and 3.3333e-3 S/m for the ML unit, ranging between 3.3333e-3 S/m and 2.5e-3 S/m for the MH unit and ranging between 2.5e-3 S/m and 5e-4 S/m for the H unit which are the electrical conductivity values equivalent to the limits of the electrical resistivity range measured for the resistivity units;

a (dimensionless) ranging between 0.5 and 0.7 for the L unit, ranging between 0.7 and 1 for the ML unit, and equal to 1 for MH and H units;

C_w = 0,1 S/m which has been assumed as a representative value for the water impregnating the deposit/rock (a low mineralized/total dissolved solids water due to poor water-rock interaction);

m (dimensionless) equal to 1.3 for L, ML, MH units and ranging between 1.3 (breccia) and 2 (bedrock) for the H unit;

S_w = 0.7 (dimensionless) which has been assumed for not fully water saturated deposit/rock;

n = 2 (dimensionless).

6. CROSS-VALIDATION OF GEOPHYSICAL RESULTS WITH OBSERVED STRATIGRAPHY

To compare resistivity units with stratigraphic aggregates, stratigraphic limits were plotted on the plane slice α (Fig. 2) extracted from the 3D block model (Figs. 10-14). Slice α lies on the same plane as the stratigraphic section a-b (main trench) (Fig. 2), which allowed correlating the two. Geophysical results are consistent with the stratigraphic section (Fig. 10) in identifying the top stratigraphic aggregates of the cave (Negrino et al., 2018) as revealed from previous archaeological surveys.

The erosional surface distinguishes the D aggregate from the underlying aggregates RB, CSB, Gr, and BM, which are well defined by the resistivity model (Figs. 10-13). The D, RB, and CSB aggregates correspond to the low resistivity unit (30 to 150 $\Omega\cdot$m, fine-grained deposits). The Gr aggregate is between the low and the middle-low resistivity unit (150 to 300 $\Omega\cdot$m fine to coarse-grained deposits) due to the presence of coarser deposits. The BM aggregate correspond to the middle-low resistivity unit (Figs. 10-13).

The D aggregate appears irregular in shape, with a heterogeneous resistivity, affected by some disturbance that disrupted the horizontal stratigraphic sequence, with a sharp, erosional contact with the underlying aggregate. Underlying aggregates appear more regular in shape, their resistivity is more homogeneous, and they display smoother contact with older aggregates.

The resistivity model fits particular stratigraphy characteristics identified from the sections exposed during excavation, such as:

- the D aggregate dips westward along slice α, but it dips southward along the northern portion of the transversal slice γ. These findings suggest a south-westward dipping of D aggregate (in this restricted area);
- the erosional surface rises slightly in the central part of slice α;
- the RB aggregate dips slightly westward along slice α; it also dips southward along the northern portion of the transversal slice γ. These findings suggest a south-westward dipping of RB aggregate (in this restricted area);
- CSB and Gr aggregates rise slightly in the west part of slice α; they also dip slightly southward along the northern portion of slice γ.

All stratigraphic aggregates show a south-westward dipping in the northeast portion of the geophysical model, at the intersection between slices α and γ. Further south, the aggregates appear to fold upwards (Figs. 10-13). In the central part of the geophysical model, the aggregates seem to be slightly bent downwards, as if to form a syncline. This is well defined by the transversal slices x and y (Fig. 9) and the 3D distribution of the low-resistivity unit merged with slices α and γ (Fig. 14).

At a local scale (along the slices), the resistivity pattern shows near continuous and slightly curved units. Some pattern distortion interrupts the continuity of the units. This could be due to the heterogeneity in the grain size distribution within the same stratigraphic aggregate, as shown for the CSB aggregate (Fig. 10). Conversely, RB and Gr aggregates may show similar resistivity values due to comparable coarse-grained deposit content (Fig. 10).

At the scale of the geophysical model, the resistivity pattern shows a discontinuous distribution of fine-grained (low resistivity) deposits (Fig. 14) and the recognition of shallow, meter-sized structures with a longitudinal orientation with respect to the primary axis of the cave.

In addition to the erosional surface exposed in excavations of the main trench, the geophysical model also identifies a sharp and irregularly shaped erosional-like surface extending along the primary axis of the cave. This structure is well defined by the resistivity pattern (Figs. 8-10, 14) where it appears as a high resistivity unit (440-2.000 Ω·m) as it is filled with mostly coarse deposits.

The cross-validation of geophysical results with observed stratigraphy supports the hypothesis mentioned above that the low-resistivity unit (30-150 Ω·m), associated with fine-grained deposits (silty-sand) represents the most promising unit from an archaeological point of view. Here, this hypothesis is based on considerations of inherent age and grain size distribution of the corresponding stratigraphic aggregate.

7. CROSS-VALIDATION OF GEOPHYSICAL RESULTS WITH ARCHAEOLOGICAL FINDINGS

The archaeological evidence collected during previous field seasons drove the hypothesis that low-resistivity units are the most promising deposits from an archaeological point of view. This can be further tested by determining if the low-resistivity units identified by this study actually correspond to the deposits where archaeological remains have been found. The discovery of a human burial in

2017 provides a good case study to test this, as part of the burial pit was still covered at the time of the geophysical survey. The Early Mesolithic burial, its accompanying grave goods, and Epigravettian artefacts located nearby were found in excavation square 2N1E (Fig. 2), which is located near the main trench, towards the entrance of the cave, at the northeast portion of the geophysical survey. These archaeological remains were found within the low-resistivity unit, which is composed mostly of fine-grained deposits (silty-sand) (Fig. 5a). The geophysical survey also shows that the burial was located in the part of the cave with the deepest fine-grained deposits (Figs. 6, 7). These geophysical findings are consistent with stratigraphic observations from the main trench.

Conversely, no archaeological remains were found in excavation squares -3N4E and -2N4E (Fig. 2), which are located far from the cave entrance, in the southeast portion of the geophysical survey. Interestingly, the low-resistivity unit does not outcrop here or outcrops with negligible thicknesses (Figs. 6, 7). Geophysical results of those squares suggest the presence of the middle-low resistivity unit (Fig. 5b) and a partially middle-high resistivity unit (Fig. 5c), which are composed of fine to coarse-grained deposits (silty-sand with gravel and sporadic blocks) and coarse-grained deposits (gravel and blocks in silty-sandy matrix), respectively.

The correlation between low resistivity units and archaeological remains discussed here supports further the hypothesis that the low-resistivity unit (30-150 Ω·m) associated with fine-grained deposits (silty-sand) represent the most promising unit from an archaeological point of view.

8. DISCUSSION

The subsurface electrical resistivity pattern allowed us to define the geometry, thickness and sediment distribution of the explorable deposits (Fig. 6), and to map the morphology of the bedrock (Fig. 7). The recognition of variable thicknesses of the loose deposits following the primary axis of the cave and increasing towards the entrance is consistent with field observations. A change in the thickness of the loose deposits has also been observed transversally from the primary axis of the cave, where the thicker part is found in the northeast portion. These findings suggest that the most significant volumes in terms of archaeological excavation are found towards the entrance of the cave on the northeast side.

The cross-validation of geophysical results with the observed stratigraphy revealed that the stratigraphic aggregates are well defined by the resistivity model. Although the resistivity pattern shows near continuous and slightly-curved units with some pattern distortion interrupting the continuity of the units at a local scale, it shows a discontinuous distribution of fine-grained (low resistivity) deposits and the recognition of shallow, meter-sized structures with a longitudinal orientation with respect to the primary axis of the cave at the larger scale. The presence of pattern distortions within individual units could be due to heterogeneity in grain size distribution.

The geophysical model also allowed the recognition of a possible sharp and irregularly shaped erosional-like surface, filled with mostly coarse deposits, which extends along the primary axis of the cave.

The cross-validation of geophysical results with the archaeological evidence collected during previous field seasons suggests that deposits associated with the low-resistivity unit, i.e., fine-grained deposits (silty-sand) are the most archaeologically promising (Figs. 5-7, 14). Although potential archaeological materials are likely to be found everywhere, fine-grained deposits are easier to dig. Therefore, these deposits might have been favored by humans when burying their dead. For this reason, we believe that the low-resistivity unit have the highest potential to contain human remains. Geophysical results thus suggest that future archaeological excavations targeting potential burials focus on the low-resistivity unit (Fig. 14), especially on the north-eastern side of the cave where this unit has greater thicknesses (Figs. 6, 7). It is worth underlining that the middle-low resistivity unit, i.e., fine to coarse-grained deposits (silty-sand with gravel and sporadic blocks) (Figs. 5, 6) also includes promising deposits as revealed by the rich Mousterian layer exposed by the excavations. In addition, as the geophysical survey did not extend to all portions of the cave, the presence of archaeological remains on the north-western side of the cave, near the entrance of the cave, cannot be excluded.

ERT proved to be an effective technique to define the geometry, thickness, volume, distribution of sediments infilling the cave, and to recognize potential archaeologically interesting structures, specifically shallow, meter-sized, fine-grained structures or pit fill-like structures (e.g., in the burial area, “human remains” in Fig. 5a). These are crucial data for designing future archaeological field surveys at Arma Veirana cave.

In this strongly heterogeneous geological setting, ERT provided an accurate model, because the electric field tends to flow mainly inside loose, in-cave deposits, which are low resistive, rather than flowing through high resistive hosting rocks. Our resistivity model may also have benefited from the 3D cave geometry. At the middle of the surveyed area, the average thickness of sediments is 1.33 m and the cave’s half-width at floor level is 4.48 m; moreover, the cave has downward diverging walls. This is consistent with findings from Olenchenko et al. (2020) who suggested that accurate resistivity models can be obtained by ERT inside a caves whose half-width is larger than the thickness of sediments and in the case of downward diverging cave walls.

This study also showed that the main drawback of the ERT method is that the properties of heterogeneous cave deposits can be characterized by a wide range of possible resistivity values depending on the heterogeneity in the grain size distribution (e.g., Schrott and Sass, 2008), as well as by actual physical and chemical states of the deposits. Furthermore, as some of these parameters are environmentally dependent (e.g., water saturation conditions), a homogeneous stratigraphic aggregate may also show resistivity variations. For these reasons, the resistivity measured in this study can vary even within the same stratigraphic aggregate or be similar for different stratigraphic aggregates. In this sense, it is worth underlining that RB and Gr aggregates may show similar resistivity values due to similar coarse-grained deposit content; conversely, the CSB aggregate appears to be affected by some disturbance that disrupts its horizontal continuity even if it is locally strongly heterogeneous. This eventuality is well shown by slices α and γ that have been cross-validated with stratigraphic observations.

As regards the application of equation (1) for the bulk total porosity estimation, although the applicability of Archie's law may be argued and is questionable for the investigated in-cave deposits, its adoption is motivated by the evidence that these materials are affected by a negligible clay content. Only the lowest resistivity deposits (approximately <100 Ω·m) included in the low-resistivity unit (30-150 Ω·m) have some clay content. However, clay-related electrical conductivity (Waxman and Smits, 1968) appears to give a negligible contribution to the bulk electrical conductivity of the materials considering that clay is dispersed in the solid matrix of the deposits.

We believe that our resistivity data are not significantly influenced by heavy-mineral composition in the sediments. Although cave sediments may represent low oxygen and chemically reducing environments, evidence of manganese oxides was found only in the BM aggregate at the base of the currently exposed stratigraphy. Field and micromorphological analyses do not indicate extensive reducing conditions in the deposits. We do not have any evidence of the manganese origin associated with a past inner-cave reducing environment; vice versa, the BM aggregate with its anthropic content suggests that manganese origin may be associated with soil humification after the human occupation of the Veirana.

As a result of anthropogenic activities, a high content of organic matter was deposited and decomposed in the typical environmental conditions of the cave vestibule, where darkness and humidity promoted the growth of saprophyte microorganisms that led to the decomposition and mineralization of organic matter, in turn generating humic acids and chelate coordination complexes, which increased metal solubility and mobility (Marìn Arroyo et al., 2008).

Due to these conditions, the evolution of the sediment itself and carbonate percolation from the surrounding rocks (the Val Tanarello limestones and the dolomitic breccia) slowed down the sediments humification, thus increasing the pH and causing the manganese precipitation in the form of oxides and hydroxides (Hill, 1982). The origin of the manganese in the BM layer may therefore be due to the degradation of its organic materials and to its later evolution as a buried anthropic sediment inside a carbonatic system subject to percolation.

8.1. Speleogenesis model of the Arma Veirana cave

Reiterating that the study of the cave and its valley are at an early stage, the data collected in the lasts years of field surveys allowed us to offer an early interpretation of its genesis and evolution.

The first consideration deals with the stratigraphy of the rock in which the cave opens and the cave mesoscale morphology: the proto-Veirana fold generated into a sedimentary sequence that runs from Late Jurassic (the Kimmeridgian-Berriasian Val Tanarello limestone) to Eocene (the "late Cretaceous-middle Paleogene" rocks of the Caprauna Formation).

Above the Val Tanarello limestone, we find a tectonic contact with a dolomitic breccia referred to as the "Brecce Dolomitiche Vacuolari" of Scitic-Anisic age; down from the Veirana entrance and from the Costa Losera flank, the evolution of the Neva valley cut away all proximal carbonatic formations, which directed the Rio Neva flow to an impermeabile substratum, the formation of the "Quarziti di Ponte di Nava" of Lopingian/Lower Triassic epoch: the contact between the "Caprauna Formation" and the physically lower "Quarziti di Ponte di Nava" is tectonic too.

Therefore, the geology of the area is very complex both for its tectonic setting and for its geomorphological evolution (Seno, 2003), but for the present study, it is important to note that the sequence of the mother-rock' fold is inverted and that the ceiling and the lateral walls of the Veirana, located inside the fold, are related to the folded strata of the "Val Tanarello limestone", locally covered by secondary carbonate depositions of the cave.

At first glance, we cannot see clear evidence of strata related to the "Caprauna Formation" inside the cave itself, which suggests that the empty space of the cave replaced the missing strata. The flanks of the fold at the cave entrance confirm this idea, as this is where we find the schists of the "Caprauna Formation" in their correct stratigraphic position and with the appropriate parasite folds.

The lack of strata of the "Caprauna Formation" inside the cave neds explaining, as it is the reason why the cave was formed. When thinking about karst systems genesis, it is easy to embrace the paradigm of the karstification by “total remover,” where carbonate caves are the result of a chemical dissolution – i.e., the physical transition of solid state compounds into a liquid phase where both the residual insoluble deposit and the dissolved elements are then carried away from water flow. However, this is not the case of the Arma Veirana, as it never had a cave river system. Therefore, we cannot refer to the cave as a “karst system” or even part of an old one.

The Arma Veirana is a “void” inside an antiform syncline. The potential energy of the system was near zero before the deepening of the rio Neva paleovalley; therefore, epigenesy could not produce the cave because the water’ very low flow rate would not have allowed the undissolved elements to be flushed out of the system. Instead, the initial solid phase was formed by the less competent rock layers that were fractured during the folding because of the high strain concentrated in the hinge region (Cosgrove, 2015). The fractured solid phase was then separated into a liquid phase that took away the soluble ions and colloids through a very low fluid flow, and then into a residual solid phase which remained in place in the form of an alterite: this latter is what we call “ghost-rock” (Quinif, 2014, 2018). The residual alterite could not go out of the system, thus fitting the concept of karstification “without total remover” (Quinif et al, 2014).

In a following stage of a cave forming through such a process, the potential energy usually grows due to some geological event like glacial rebound, eustatic regression and so on. In the case of the paleo-Veirana, the potential energy likely grew due to to the deepening of the Rio Neva paleovalley: in such a situation, the residual solid phase may have been removed by “piping” phenomena with the genesis of a suffusion cave stage (Bartolomé et al, 2015).

We are still evaluating the role of the paleo-Neva in the removal of the “ghost rock” from the cave: we do not have yet any evidence of an ingression of the rio Neva inside the cave, but it is clearly possible. In addition, the morphological regularity of the bedrock made visible by our geophysical model could be related to an erosion surface generated by water flow during the deepening of the valley. In this sense, the gully-like morphology that we see in our geophysical model is of particular significance if we think that the survived vertical strata beds of different competence, at the bottom of the cave, were subjected to an erosional water sheet flow inside the open fold after the pseudokarst genetical stages formerly suggested. There are similar situations described in other caves of this kind, like the Ladies Cave Anticline at Sandersfoot (Pembrokeshire, UK), the Cave of Harpea (Basque Country, Pyrenees) and the Anticline Cave at Wellington (Australia): the last one is an hypogene multiphase cave (Osborne, 2010). However, to confirm and clarify all the hypothesized ideas presented here, we need to perform more field studies. In particular, we plan on creating a geological trench far from the archeological deposits, which will uncover the "bedrock," thus allowing us to evaluate its geological characteristics more precisely.

9. CONCLUSIONS

We presented the 3D Electrical Resistivity Tomography (ERT) imaging of the archaeological deposits at Arma Veirana cave (Northern Italy), to date only partially explored during a series of four archaeological field seasons.

We obtained the subsurface electrical resistivity pattern with the main aims to define the geometry, thickness and sediment distribution features of the deposits, and map the morphology of the underlying bedrock. This study revealed that the thickness of the deposits is variable along the primary axis of the cave and ranges between more than 1.5 meters towards the entrance of the cave to less than 10 centimetres towards its innermost part, where they show a discontinuous distribution. A change in the thickness of the deposits has also been revealed transversely to the primary axis of the cave, with a thickening towards the northeast side of it. The study allowed the recognition of shallow, meter-sized, fine-grained sediment filled structures with a longitudinal orientation with respect to the primary axis of the cave, as well as a possible erosional-like structure, filled with mostly coarse deposits, which extends along the primary axis of the cave.

The results of the geophysical survey were cross-validated with the exposed stratigraphy as well as with the presence of archaeological material culture. Both cross-validation supported the hypothesis that the low-resistivity unit, which includes fine-grained structures, is the most archaeologically promising. The results also suggest that the middle-low resistivity unit can also be linked to rich archaeological layers.

These results will be useful to design future archaeological surveys at Arma Veirana cave and they provide further insights on 3D ERT applicability and effectiveness in investigating any in-cave deposits. Although ERT has rarely been employed in Paleolithic cave contexts because Paleolithic remains are typically disseminated in loose deposits and either do not possess high electrical resistivity contrasts or are too small to be detected, an accurate resistivity model was obtained in this study. Even though this model did not recognize any specific remains, it defined the properties and volume of the explorable deposits and identified the most promising areas to excavate, i.e., likely artefact-bearing deposits.

As regards the issues deriving from the application of ERT in such confined cave environment, the results of our study are consistent with previous findings that accurate resistivity models can be obtained by ERT inside a cave whose half-width is larger than the thickness of sediments and in the case of downward diverging cave walls.

Acknowledgements

The authors are grateful to the “Soprintendenza Archeologia, Belle Arti e Paesaggio per la città metropolitana di Genova e le province di Imperia, La Spezia e Savona”, in the persons of the Superintendent Vincenzo Tiné and the official-archaeologist Marta Conventi for allowing us to access and sample the cave and for their support. We also thank Federico Borsari for his support in data processing and editing.

Archaeological field excavations at Arma Veirana were funded by The Wenner-Gren Foundation, Leakey Foundation, National Geographic Society Waitt Program (W391-15), Hyde Family Foundation [via the Human Origins Migrations and Evolutionary Research (HOMER) consortium], Social Sciences and Humanities Research Council (SSHRC) Insight Development Grant #430-2018-00846, University of Colorado Denver, Washington University.

The authors wish to thank the Editor-in-Chief Neil Roberts, the Editor for Europe Achim Brauer and two anonymous referees who kindly reviewed the earlier version of this manuscript and provided valuable suggestions and comments, greatly improving the quality of the manuscript.

Supplementary Data

Data used in this study are available on Zenodo, http://doi.org/10.5281/zenodo.4544550, (Torrese et al., 2021b).

References

Abu Zeid, N, Bignardi, S., Russo, P., Peresani, M., 2019. Deep in a Paleolithic archive: Integrated geophysical investigations and laser-scanner reconstruction at Fumane Cave, Italy. Journal of Archaeological Science: Reports, 27, 101976, ISSN 2352-409X, https://doi.org/10.1016/j.jasrep.2019.101976.

Archie, G.E., 1942. The electrical resistivity log as an aid in determining some reservoir characteristics. Journal of Petroleum Technology 1, 55−62.

Astin, T., Eckardt, H., Hay, S., 2007. Resistivity imaging survey of the Roman Barrows at Bartlow, Cambridgeshire, UK. Archeological Prospection, 14: 24– 37.

Al-Zoubi, A. S., Abueladas, A. E. R. A., Al-Rzouq, R. I., Camerlynck, C., Akkawi, E., Ezarsky, M., … Al Rawashdeh, S. (2007). Use of 2D multi electrodes resistivity imagining for sinkholes hazard assessment along the eastern part of the Dead Sea, Jordan. American Journal of Environmental Sciences, 3(4), 229–233. https://doi.org/10.3844/ajessp.2007.230.234

Bartolomé, M., Sancho, C., Moreno, A., Oliva-Urcia, B,, Belmonte, A., Bastida, J., Cheng, H., Edwards, R.L., 2015. Upper Pleistocene interstratal piping-cave speleogenesis: The Seso Cave System (Central Pyrenees, Northern Spain), Geomorphology, Vol.228, 1th January 2015, 335-344

Beck, A., Weinstein-Evron, M., 1997. A geophysical survey in the el-Wad cave, Mount Carmel, Israel. Archaeological Prospection, 4 (2), pp. 85-91. 10.1002/(SICI)1099-0763(199706)4:23.3.CO;2-3

Becker, R.J., Janković, I., Ahern, J.C.M., Komšo, D., 2019. High data density electrical resistivity tomography survey for sediment depth estimation at the Romuald's Cave site. Archaeological Prospection. 2019; 26: 361– 367. https://doi.org/10.1002/arp.1749

Berge, M.A., Drahor, M.G., 2011a. Electrical resistivity tomography investigations of multilayered archaeolog-ical settlements: part I – modelling. Archaeological Prospection, 18: 159–171.

Berge, M.A., Drahor, M.G., 2011b. Electrical resistivity tomography investigations of multilayered archaeolog-ical settlements: part II – a case study from Old SmyrnaHöyük, Turkey. Archaeological Prospection, 18: 291–302.

Bertock, C., Martire, L., Perotti, E., d'Atri, A., & Piana, F. (2011). Middle-Late Jurassic syndepostional tectonics recorded in the Ligurian Briançonnais succession (Marguareis-Mongioie area, Ligurian Alps, NW Italy). Swiss Journal of Geosciences, 104, 237–255.

Campana, S., and Piro, S., 2008. Seeing the Unseen. Geophysics and Landscape Archaeology (1st ed.). CRC Press. https://doi.org/10.1201/9780203889558

Cardarelli, E., Di Filippo, G., Tuccinardi, E., 2006. Electrical resistivity tomography to detect buried cavities in Rome: a case study. Near Surf Geophys 4:387–392

Carrière, S. D., Chalikakis, K., Sénéchal, G., Danquigny, C., & Emblanch, C. (2013). Combining Electrical Resistivity Tomography and Ground Penetrating Radar to study geological structuring of karst Unsaturated Zone. Journal of Applied Geophysics, 94, 31–41. https://doi.org/10.1016/j.jappgeo. HYPERLINK "https://doi.org/10.1016/j.jappgeo.2013.03.014"2013.03.014

Cosgrove, J.W., 2015. The association of folds and fractures and the link between folding, fracturing and fluid flow during the evolution of a fold-thrust belt: a brief review, in: Richards, F. L., Richardson, N. J., Rippington, S. J., Wilson, R. W. & Bond, C. E. (eds) Industrial Structural Geology: Principles, Techniques and Integration. Geological Society, London, Special

Publications, 421, http://dx.doi.org/10.1144/SP421.11

Cozzolino, M., Caliò, L.M., Gentile, V., Mauriello, P., and Di Meo, A., 2020, The Discovery of the Theater of Akragas (Valley of Temples, Agrigento, Italy): An Archaeological Confirmation of the Supposed Buried Structures from a Geophysical Survey. Geosciences 2020, 10(5),161; https://doi.org/10.3390/geosciences10050161

Dahlin, T., & Loke, M. H., 1998. Resolution of 2D Wenner resistivity imaging as assessed by numerical modelling. Journal of Applied Geophysics, 38(4), 237–249. https://doi.org/10.1016/S0926-98 HYPERLINK "https://doi.org/10.1016/S0926-9851(97)00030-X"51(97)00030-X

Dal Bo, G., Laiolo, G., Lazzarini, G., 1978. L'Arma di Costa di Cerisola, "Stalattiti e stalagmiti – Gruppo Speleologico Savonese" 16, 14 (in Italian).

Dallagiovanna, G., Gaggero, L., Seno, S., Felletti, F., Mosca, P., Decarlis, A., Pellegrini, L., Poggi, F., Bottero, D., 2011. Note Illustrative della Carta Geologica d'Italia alla scala 1:50.000, foglio 228, Cairo Montenotte. ISPRA – Servizio Geologico d'Italia.

Decarlis, A. & Lualdi, A., 2009. A sequence stratigraphic approach to a Middle Triassic shelf-slope complex of the Ligurian Alps (Ligurian Brianconnais, Monte Carmo-Rialto unit, Italy). Facies, volume 55, Article number: 267.

Deiana, R., Bonetto, J. & Mazzariol, A., 2018. Integrated Electrical Resistivity Tomography and Ground Penetrating Radar Measurements Applied to Tomb Detection. Surv Geophys 39, 1081–1105. https://doi.org/10.1007/s10712-018-9495-x

Dellagiovanna, G., Gaggero, L., Seno, S., Felletti, F., Mosca, P., Decarlis, A., Pellegrini, L., Poggi, F., Bottero, D., 2011. Note Illustrative della Carta Geologica d'Italia alla scala 1:50000, foglio 228, Cairo Montenotte. ISPRA-Servizio Geologico d'Italia.

de la Vega, M., Osella, A., and Lascano, E., 2003, Joint inversion of Wenner and dipole-dipole data to study a gasoline-contaminated soil. Journal of Applied Geophysics, 54(1-2): 97-109.

Dubois, C., Lans B., Kaufman, O., Maire, R., Quinif, Y, 2011. Karstification de type fantomes de roche en Entre-deux-Mers (Gironde, France): Implications en karstogenèse et morphologie karstique. Karstologia: revue de karstologie et de spéléologie physique, n.57, 1er semester, 19-27. https://www.persee.fr/doc/karst_0751-7688_2011_num_57_1_2690

Drahor, M.G., Berge, M.A., Kurtulmus, T.Ö., Hartmann, M., Speidel, M.A., 2008. Magnetic and electrical resistivity tomography investigations in a Roman legionary camp site (Legio IV Scythica) in Zeugma, Southeastern Anatolia, Turkey. Archaeological Prospection 15: 159–186.

El-Qady, G., Metwaly, M., Drahor, M.G., 2019. Geophysical techniques applied in archaeology. In Archaeogeophysics: State of the Art and Case Studies. Cham: Springer, pp. 1–25.

Fikos, I., Vargemezis, G., Pennos, C., Lønøy, B., Jensen, K., Tveranger, J., 2019. Processing 2D ERT

Data in 3D Environment-A Case Study Inside a Karstic Cave in Greece. 25th European Meeting of Environmental and Engineering Geophysics, Volume 2019, p.1 – 5, https://doi.org/10.3997/2214-4609.201902389

Goudie A. S., 2013. Encyclopedia of Geomorphology, Vol. I, International Association of Geomorphologists, Routledge.

Goldberg, P., and Sherwood, S.C., 2006. Deciphering human prehistory through the geoarcheological study of cave sediments. Evol. Anthropol., 15: 20-36. https://doi.org/10.1002/evan.20094

Griffiths, D. H., & Barker, R. D., 1993. Two-dimensional resistivity imaging and modelling in areas of complex geology. Journal of Applied Geophysics, 29(3–4), 211–226. https://doi.org/10.1016/0926-9851(93)90005-J

Guerin, R., & Benderitter, Y., 1995. Shallow karst exploration using MT-VLF and DC resistivity methods. Geophysical Prospecting, 43(5), 635–653. https://doi HYPERLINK "https://doi.org/10.1111/j.1365-2478.1995.tb00272.x".org/10.1111/j.1365-2478.1995.tb00272.x

Hancock, A.J, 1999. An investigation of the soils and sediment contained within the entrance chamber (or The Vestibule), Peak Cavern, and the assessment of their archaeological significance through the integration of geophysical techniques. BSc Project, Department of Archaeological Sciences, University of Bradford, 71pp.

Hill C.A., 1982. Origin of black deposits in caves. National Speleological Society Bulletin, 44, 15-19.

Hirniak, J. N., Smith, E. I., Johnsen, R., Ren, M., Hodgkins, J., Orr, C., Negrino, F., Riel-Salvatore J., Fitch, S., Miller, C. E., Zerboni, A., Mariani, G. S., Harris, J. A., Gravel-Miguel, C., Strait, D., Peresani, M., Benazzi, S., Marean, C. W., 2020. Discovery of cryptotephra at Middle–Upper Paleolithic sites Arma Veirana and Riparo Bombrini, Italy: a new link for broader geographic correlations, Journal of Quaternary Science 35 (1-2), 199–212.

Hodgkins, J., Orr, C.M., Gravel-Miguel, C., Riel-Salvatore, J., Miller, C.E., Bondioli, L., Nava, A., Lugli, F., Talamo, S., Hajdinjak, M., Cristiani, E., Romandini, M., Meyer, D., Drohobytsky, D., Kuester, F., Pothier Bouchard, G., Buckley, B., Mancini, L., Baruffaldi, F., Silvestrini, S., Arrighi, S., Keller, H.M., Griggs, R.B., Peresani, M., Strait, D.S., Benazzi, S., Negrino, F., In review. Infant funerary rites and female personhood in early Mesolithic Europe.

Jol, H.M., Schroder, J.F., Reeder, P., Freund, R.A., 2002. Return to the Cave of Letters (Israel): a ground penetrating radar archaeological expedition. D.A. Noon, G.F. Stickley, D. Longstaff (Eds.), Proceedings of the Eighth International Conference on Ground Penetrating Radar (GPR 2000). SPIE 4084 (2002), pp. 882-886

LaBrecque, D. J., 1996. The effects of noise on Occam's inversion of resistivity tomography data. Geophysics, 61(2), 538. https://doi.org/10.11 HYPERLINK "https://doi.org/10.1190/1.1443980"90/1.1443980

Laigre, L., Reynards, E., Arnaud-Fassetta, G., Baron, L., Glenz, D., 2012. Characterisation of the Rhône river palaeodynamics in Central Valais (Switzerland) with the electrical resistivity tomography method. Géomorphol Relief Processus Environ 4:405–426

Loke, M. H., Acworth, I., & Dahlin, T., 2003. A comparison of smooth and blocky inversion methods in 2D electrical imaging surveys. Exploration Geophysics, 34(3), 182–187. https://doi.org/10.10 HYPERLINK "https://doi.org/10.1071/EG03182"71/EG03182

Loke, M. H., & Barker, R. D., 1996. Rapid least-squares inversion of apparent resistivity pseudosections by a quasi-Newton method. Geophysical Prospecting, 44(1), 131–152. https://doi.org/10.1111/j.1365-2478.1996.tb00142.x

Maillol, J. M., Seguin, M. K., Gupta, O. P., Akhauri, H. M., & Sen, N. (1999). Electrical resistivity tomography survey for delineating uncharted mine galleries in West Bengal, India. Geophysical Prospecting, 47(2), 103–116. https://d HYPERLINK "https://doi.org/10.1046/j.1365-2478.1999.00126.x"oi.org/10.1046/j.1365-2478.1999.00126.x

Mallol, C., and Goldberg, P., 2017. Caves and Rockshelter Sediments. In C. Nicosia and G. Stoops (eds.), Archaeological Soil and Sediment Micromorphology. Hoboken, NJ: Wiley, pp. 359-377.

Marìn Arroyo, A.B., Landete Ruiz, M.D., Vidal Bernabeu, G., Seva Romàn, R., Gonzàles Morales, M.R., Straus, L.G., 1982. Archaeological implications of human-derived manganese coatings: a study of blackened bones in El Miròn Cave, Cantabrian Spain, Journal of Archaeological Science 35, 801-813.

Matias, H.C., Monteiro Santos, F.A., Rodrigues Ferreira, F.E., Machado, C., Luzio, R., 2006. Detection of graves using the micro-resistivity method. Ann. Geophys. Vol. 49 No. 6 https://doi.org/10.4401/ag-3102

Morelli, G., & LaBrecque, D. J., 1996. Advences in ERT inverse modeling. European Journal of Environmental and Engineering Geophysics, 1, 171–186.

Negrino, F., Benazzi, S., Hodgkins, J., Miller, C., E., Orr, C., Peresani, M., Riel-Salvatore, J., Strait, D., De Santis, H., 2018. Erli (SV). Arma Veirana, in Archeologia in Liguria, Nuova Serie, VI, 2014-2015, Soprintendenza Archeologia, Belle Arti e Paesaggio per la città metropolitana di

Genova e le province di Imperia, Savona e La Spezia, Genova, 460-461.

Oberender, P. & Plan, L., 2018. A genetic classification of caves and its application in eastern Austria. From: Advances in Karst Research: Theory, Fieldwork and Applications, Geological Society, London, Special Pubblications, 466, 121-136.

Obradovic, M., Abu Zeid, N., Bignardi, S., Bolognesi, S., Peresani, M., Russo, P., and Santarato, G., 2015, High Resolution Geophysical and Topographical Surveys for the Characterisation of Fumane Cave Prehistoric Site, Italy: Near Surface Geoscience 2015: 21st European Meeting of Environmental and Engineering Geophysics, https://doi.org/10.3997/2214-4609.201413676.

Olenchenko, V., Tsibizov, L., Osipova, P., 2019. Electrotomography in a cave: a numerical experiment. Interexpo GEO-Siberia 2(2):111-115. DOI: 10.33764/2618-981X-2019-2-2-111-115 Papadopoulos, N.G., Yi, M.-J., Kim, J.-H., Tsourlos, P., Tsokas, G.N., 2010. Geophysical investigation of tumuli by means of surface 3D electrical resistivity tomography. Journal of Applied Geophysics 70: 192– 205.

Olenchenko, V.V., Tsibizov, L.V., Osipova, P.S., Chargynov, T.T., Viola B.T., Kolobova K.A., Krivoshapkin A.I., 2020. Peculiarities of Using 2D Electrical Resistivity Tomography in Caves. Archaeology, Ethnology & Anthropology of Eurasia, 48(4):67-74. https://doi.org/10.17746/1563-0110.2020.48.4.067-074

Ortega, A.I., Benito-Calvo, A., Porres, J., Pérez-González, A, Martín Merino, M.A., 2010. Applying electrical resistivity tomography to the identification of endokarstic geometries in the Pleistocene Sites of the Sierra de Atapuerca (Burgos, Spain). Archaeol. Prospect., 17, pp. 233-245, 10.1002/arp.392

Osborne R.A.L., 2010. Rethinking eastern Australian caves. Geological Society, London, Special Publications 2010; v.346; 289-308

Osipova, P.S., Olenchenko, V.V., Tsibizov, L.V., and Krivoshapkin, A.I., 2020. The Study of

Paleolithic Monuments in Karst Caves by Electrotomography. Engineering and Mining Geophysics 2020, Volume 2020, p.1 – 8.

Papadopoulos, N., Tsourlos, P., Tsokas, G., & Sarris, A., 2006. Two-dimensional and three-dimensional resistivity imaging in archaeological site investigation. Archaeological Prospection, 13(3), 163181.

Papadopoulos, N.G., Tsourlos, P., Tsokas, G.N., Sarris, A., 2007. Efficient ERT measuring and inversion strategies for 3D imaging of buried antiquities. Near Surf. Geophys. 2007, 5, 349–362.

Papadopoulos, N.G, Yi, M-J., Kim, J-H., Tsourlos, P., Tsokas, G.N., 2010. Geophysical investigation of tumuli by means of surface 3D Electrical Resistivity Tomography, Journal of Applied Geophysics, Volume 70, Issue 3, Pages 192-205, ISSN 0926-9851, https://doi.org/10.1016/j.jappgeo.2009.12.001.

Papadopoulos, N.G., Sarris, A., Parkinson, W.A., Gyucha, A., Yerkes, R.W., Duffy, P.R., Tsourlos, P., 2014.
Electrical Resistivity Tomography for the Modelling of Cultural Deposits and Geomophological Landscapes at Neolithic Sites: a Case Study from Southeastern Hungary. Archaeol. Prospect., 21, 169-183, DOI: 10.1002/arp.1480

Piroddi, L., Calcina, S.V., Trogu, A., Ranieri, G., 2020. Automated Resistivity Profiling (ARP) to explore wide
archaeological areas: The prehistoric site of Mont'e Prama, Sardinia, Italy. Remote Sens. 2020, 12, 461.

Pringle, J. K., Westerman, A. R., Schmidt, A., Harrison, J., Shand ley, D., Beck, J., Donahue, R. E. and Gardiner, A. R., 2002. Investigating Peak Cavern, Castleton, Derbyshire, UK: integrating cave survey, geophysics, geology and archaeology to create a 3-D digital CAD model. Cave and Karst Science, 29(2), 67-74.

Quarto, R., Schiavone, D., Diaferia, I., 2007. Ground penetrating radar survey of a prehistoric site in

Southern Italy. J. Archaeol. Sci., 34, pp. 2071-2080.
Quinif, Y., 2014. La fantomisation – Une nouvelle manière de concevoir la formation des cavernes. Regards N.79 – Deuxieme semester, 42-72.
Quinif, Y., 2018. Fantomisation et spéléogenèse: implications et questionnement. Karstologia: revue de karstologie et de spéléologie physique, n.69, 32-46
Quinif, Y. & Bruxelles, L., 2011. L'altération de type "fantome de roche": processus, évolution et implications pour la karstification. Gèomorphologie: relief, processus, environment, Vol.17 – n.4, 349-358.
Kneisel, C., 2006. Assessment of subsurface lithology in mountain environments using 2D resistivity imaging. Geomorphology, 80(1–2), 32–44. https://doi.org/10.1016/j.geomorph.2005.09.012
Rainone, M. L., Rusi, S., & Torrese, P., 2015. Mud volcanoes in central Italy: Subsoil characterization through a multidisciplinary approach. Geomorphology, 234, 228–242. https://doi.org/10.1016/j.geomorph.2015.01.026
Ramsey, C.B., 2009. Bayesian analysis of radiocarbon dates. Radiocarbon 51, 337-360.
Reimer, P.J., Austin, W.E.N., Bard, E., Bayliss, A., Blackwell, P.G., Bronk Ramsey, C., Butzin, M., Cheng, H., Edwards, R.L., Friedrich, M., Grootes, P.M., Guilderson, T.P., Hajdas, I., Heaton, T.J., Hogg, A.G., Hughen, K.A., Kromer, B., Manning, S.W., Muscheler, R., Palmer, J.G., Pearson, C., Van der Plicht, J., Reimer, R.W., Richards, D.A., Scott, E.M., Southon, J.R., Turney, C.S.M., Wacker, L., Adolphi, F., Büntgen, U., Capano, M., Fahrni, S.M., Fogtmann-Schulz, A., Friedrich, R., Köhler, P., Kudsk, S., Miyake, F., Olsen, J., Reining, F., Sakamoto, M., Sookdeo, A., Talamo, S., 2020. The IntCal20 Northern Hemisphere radiocarbon age calibration curve (0–55 cal kBP). Radiocarbon 62, 725-757.
Rezaee, M.R., Motiei, H., and Kazemzadeh, E., 2007. A new method to acquire m exponent and tortuosity factor for microscopically heterogeneous carbonates. Journal of Petroleum Science and Engineering. 56 (4): 241-251.
Salem, H.S., and Chilingarian, G.V., 1999. The cementation factor of Archie's equation for

shaly sandstone reservoirs: Journal of Petroleum Science and Engineering, March, pp. 83–93.

Sarris, A., Kalayci, T., Moffat, I., Manataki, M., 2018. An Introduction to Geophysical and Geochemical Methods in Digital Geoarchaeology. In: Siart C., Forbriger M., Bubenzer O. (eds) Digital Geoarchaeology. Natural Science in Archaeology. Springer, Cham. https://doi.org/10.1007/978-3-319-25316-9_14

Sarris, A., Papadopoulos, N., Soupios, S., 2014. Contribution of geophysical approaches to the study of Priniatikos Pyrgos. In: Molloy BPC, Duckworth CN (eds) A cretan landscape through time: Priniatikos Pyrgos and environs, BAR International Series, vol 2634. Archaeopress, Oxford, pp 61–69

Satitpittakul, A., Vachiratienchai, C., & Siripunvaraporn, W. (2013). Factors influencing cavity detection in Karst terrain on two-dimensional (2-D) direct current (DC) resistivity survey: A case study from the western part of Thailand. Engineering Geology, 152(1), 162–171. https://doi.org/10.1016/j.enggeo.2012.10.015

Sauro, U., 2005. Closed Depressions. From: Culver, D.C. & White, W.B., Encyclopedia of Caves. Elsevier Academic Press, Burlington-London, 108-122

Scapozza, C., Laigre, L., 2014. The contribution of electrical resistivity tomography (ERT) in Alpine dynamics geomorphology: case studies from the Swiss Alps. Géomorphol Relief Processus Environ 20(1):27–42

Schmidt, A.R., Linford, P., Linford, N., David, A., Gaffney, C.F., Sarris, A., and Fassbinder, J., 2015.

EAC Guidelines for the use of Geophysics in Archaeology: Questions to Ask and Points to Consider. EAC Guidelines 2. Namur, Belgium: Europae Archaeologia Consilium (EAC), Association Internationale sans But Lucratif (AISBL). ISBN 978-963-9911-73-4. 135p.

Schrott, L., & Sass, O., 2008. Application of field geophysics in geomorphology: Advances and limitations exemplified by case studies. Geomorphology, 93(1–2), 55–73. https://doi.org/10.1016/j.geomorph HYPERLINK "https://doi.org/10.1016/j.geomorph.2006.12.024".2006.12.024

Seaton, W. J. and Burbey, T. J., 2002. Evaluation of two-dimensional resistivity methods in a fractured crystalline-rock terrane. Journal of Applied Geophysics, 51(1): PII S0926-9851(02)00212-4. DOI: 10.1016/S0926-9851(02)00212-4

Seno, S., Dallagiovanna, G., and Vanossi, M., 2003. Palaeogeography and thrust development in the Pennidic Domain of the Western Alpine chain: examples from the Ligurian Alps. Boll.Soc.Geol. It., 122 (2003), 223-232

Shopov, Y., Stoykova, D., Petrova, A., Vasilev, V., Tsankov, L., 2008. Potential and limitations of the archaeo-geophysical techniques. R.I. Kostov, B. Gaydarska, M. Gurova (Eds.), Proceedings of the International Conference, 29–30 October 2008, Geoarchaeology and Archaeomineralogy, Sofia, Publishing House “St. Ivan Rilski”, Sofia, pp. 320-324.

Simyrdanis, K., Papadopoulos, N, Kim, J.H., Tsourlos, P., Moffat, I., 2015. Archaeological investigations in the shallow seawater environment with electrical resistivity tomography. Surf Geophys 13:601–611.

Sola, F., 2007. Tesi di Laurea: Geomorfologia carsica del monte Fenera (Vc). Relatore prof. Alfredo Bini, correlatore dr. Stefano Turri, Università degli Studi di Milano – Facoltà di Scienze Matematiche, Fisiche e Naturali, Corso di Laurea in Scienze Geologiche, A.A. 2006-2007 (in Italian, unpublished)

Smith, D. L. (1986). Application of the pole-dipole resistivity tecnnique to the detection of solution cavities beneath highways. Geophysics, 51(3), 833–837. https://doi.org/10.1190/1.1442135

Supriyadi, A., Suprianto, A., Priyantari, N., Cahyono, B.E., Sholeha, I., 2019. Assessment of validated geoelectrical resistivity methods to reconstruct buried archaeological site (case study: Beteng Site-Sidomekar, Jember Regency). J. Phys. Conf. Ser., 1153, 012026.

Szalai, S., Novak, A., & Szarka, L., 2009. Depth of Investigation and Vertical Resolution of Surface Geoelectric Arrays. Journal of Environmental & Engineering Geophysics, 14(1), 15–23. https://doi.org/10.2113/JEEG14.1.15

Szalai, S., & Szarka, L. (2008). Parameter sensitivity maps of surface geoelectric arrays I. Linear arrays. Acta Geodaetica et Geophysica Hungarica, 43(4), 419–437. https://doi.org/10.1556/AGeod.43.2008.4.4

Thacker, P.T., Ellwood, B.B., Pereira, C.M.C., 2002. Detecting Palaeolithic Activity Areas Through Electrical Resistivity Survey: An Assessment from Vale de Óbidos, Portugal, Journal of Archaeological Science, Volume 29, Issue 6, Pages 563-570, ISSN 0305-4403, https://doi.org/10.1006/jasc.2001.0691.

Tonkov, N., 2014. Geophysical survey at the early Neolithic site of Yabalkovo. In: Roodenberg J, Leshtakov K, Petrova V (eds) Yabalkovo vol 1, ATE- Ars et Technica Expicatus, Sofia Univeristy "St. Kliment Ohridski", Sofia, pp 73–78

Torrese P., 2020. Investigating karst aquifers: Using pseudo 3-D electrical resistivity tomography to identify major karst features. Journal of Hydrology, 580, doi.org/10.1016/j.jhydrol.2019.124257

Torrese, P., Pozzobon, R., Rossi, A.P., Unnithan, V., Sauro, F., Borrmann, D., Lauterbach, H., Santagata, T., 2021a. Detection, imaging and analysis of lava tubes for planetary analogue studies using electric methods (ERT), Icarus, 357, doi.org/10.1016/j.icarus.2020.114244.

Torrese P., Zucca F., Martini S., Benazzi S., Drohobytsky D., Gravel-Miguel C., Hodgkins J., Meyer D., Miller C., Peresani M., Orr C., Riel-Salvatore J., Strait D.S., Negrino, F., 2021b. 3D electrical resistivity data collected at Arma Veirana cave (Northern Italy) [Data set]. Zenodo. http://doi.org/10.5281/zenodo.4544550.

Tsokas, G.N., Tsourlos, P.I., Stampolidis, A., Katsonopoulou, D., Soter, S., 2009. Tracing a major Roman road in the area of ancient Helike by resistivity tomography. Archaeological Prospection 16: 251– 266.

Tsokas, G.N., Tsourlos, P.I., Kim, J.H., Yi, M.J., Vargemezis, G., Lefantzis, M., Fikos, E., Peristeri, K., 2018. ERT imaging of the interior of the huge tumulus of Kastas in Amphipolis (northern Greece).

Archaeol. Prospect., 25, 347–361.
Van Schoor, M., 2002. Detection of sinkholes using 2D electrical resistivity imaging. Journal of Applied Geophysics, 50(4), 393–399. https://do HYPERLINK "https://doi.org/10.1016/S0926-9851(02)00166-0"i.org/10.1016/S0926-9851(02)00166-0
Yogeshwar, P., Hamacher, S., Reçi, H., Hauck, T., Onuzi, K., Tezkan, B., 2019. Investigating Sedimentological Architecture Using Electrical Resistivity Tomography: A Case Study from the Archaeological Open-Air Site Shën Mitri, Southern Albania. Pure Appl. Geophys. 176, 843–856. https://doi.org/10.1007/s00024-018-1987-6
Zhu, J., Currens, J. C., & Dinger, J. S., 2011. Challenges of using electrical resistivity method to locate karst conduits-A field case in the Inner Bluegrass Region, Kentucky. Journal of Applied Geophysics, 75(3), 523–530. https://doi.org/10.1016/j.jappgeo.2011.08.009
Waxman, M.H., Smits, L.J.M., 1968. Electrical Conductivities in Oil-Bearing Shaly Sands. SPE J. 8: 107–122. doi: https://doi.org/10.2118/1863-A
Witten, A., 2017. Handbook of Geophysics and Archaeology. New York: Routledge.

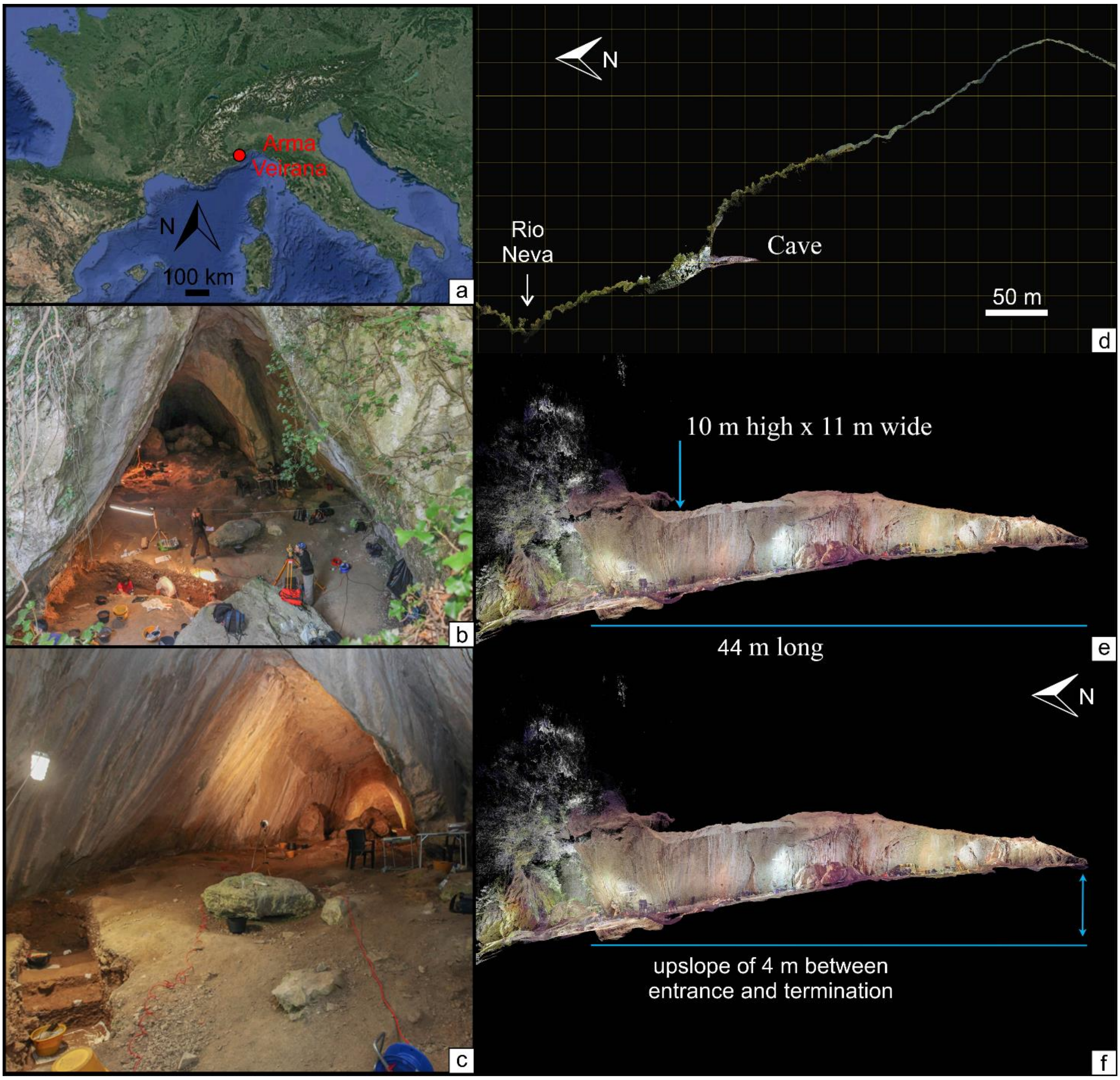

Fig. 1: Arma Veirana: (a) geographical setting, (b) picture from outside the cave, (c) picture from inside the cave, (d) location of the cave in cross section with respect to the slope and Rio Neva, (e, f) cross section and geometric features of the cave; the cross sections (d-f) were derived from a LiDAR reconstruction of the cave.

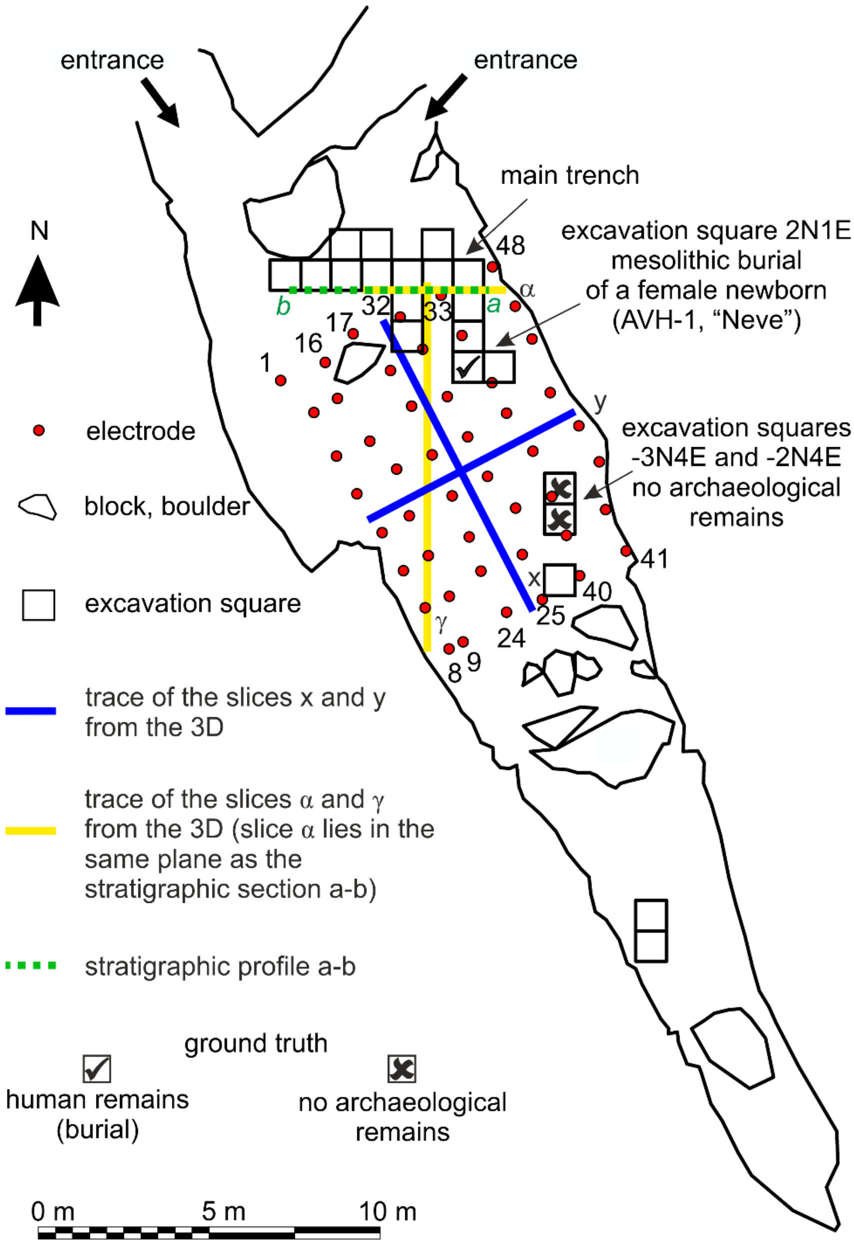

Fig. 2: Experimental layout of the 3D ERT survey along with the traces of the slices and of the stratigraphic profiles, location of excavation pits and main archaeological material.

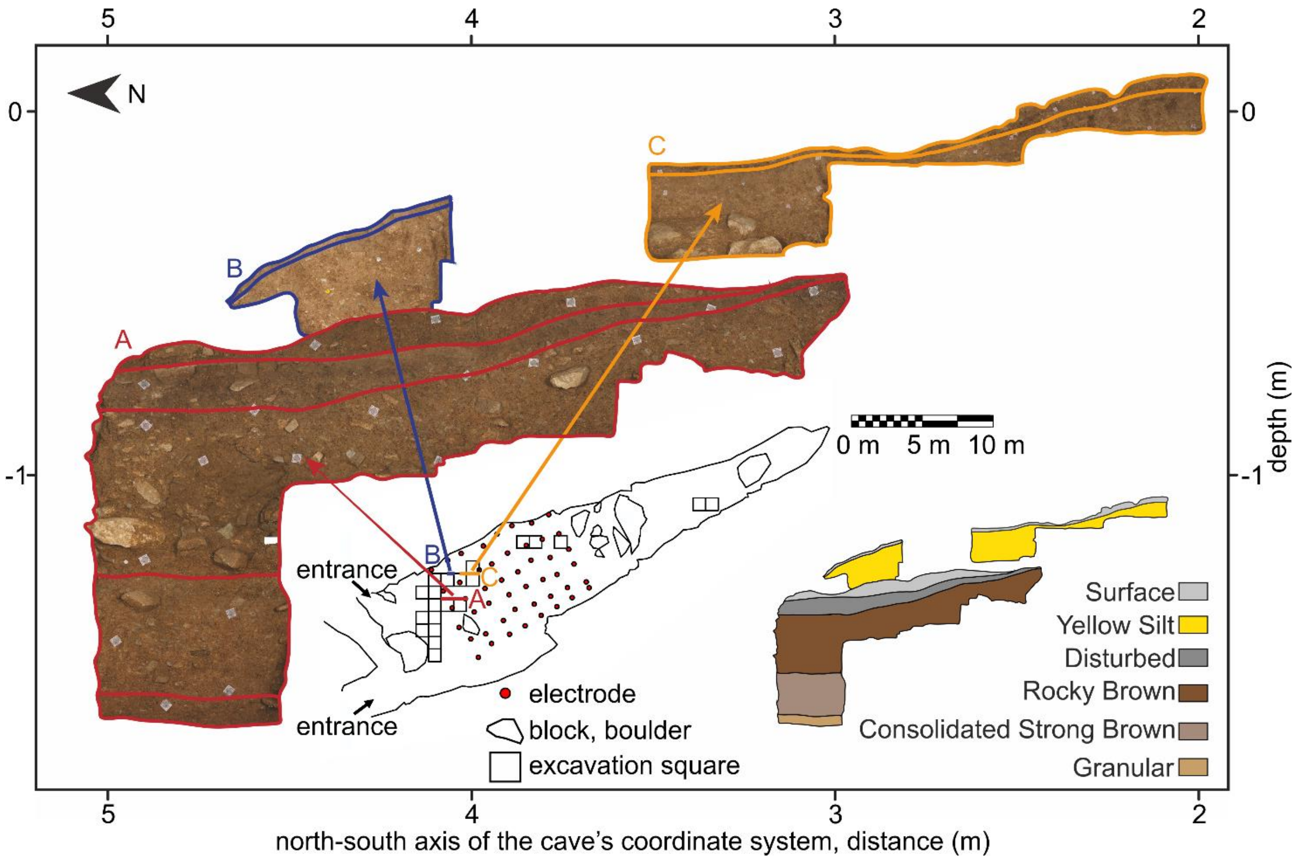

Fig. 3: Photograph and stratigraphic drawing of N-S profile. The composite image is a projection of two profiles. The more western profile is located closer to an erosional rill, and therefore does not contain Yellow Silt (YS) aggregate, which is only exposed in excavations along the flank of the cave as represented in the more eastern profile. Excavations have exposed deposits (Black Mousterian, BM) below Granular (GR), but they have not been reached yet in the excavation units.

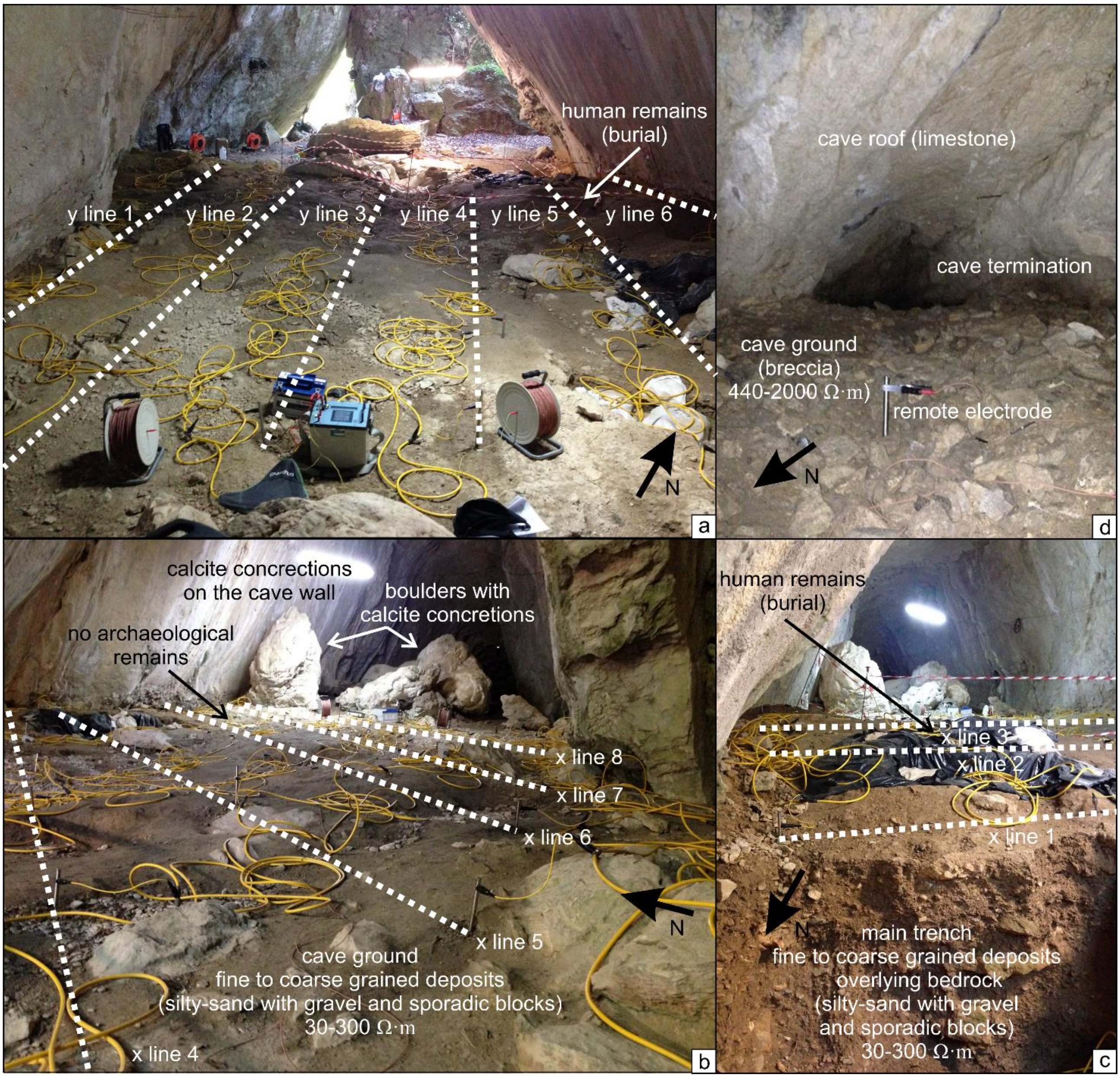

Fig. 4: Pictures showing different views of the 3D ERT survey grid along with lithological description.

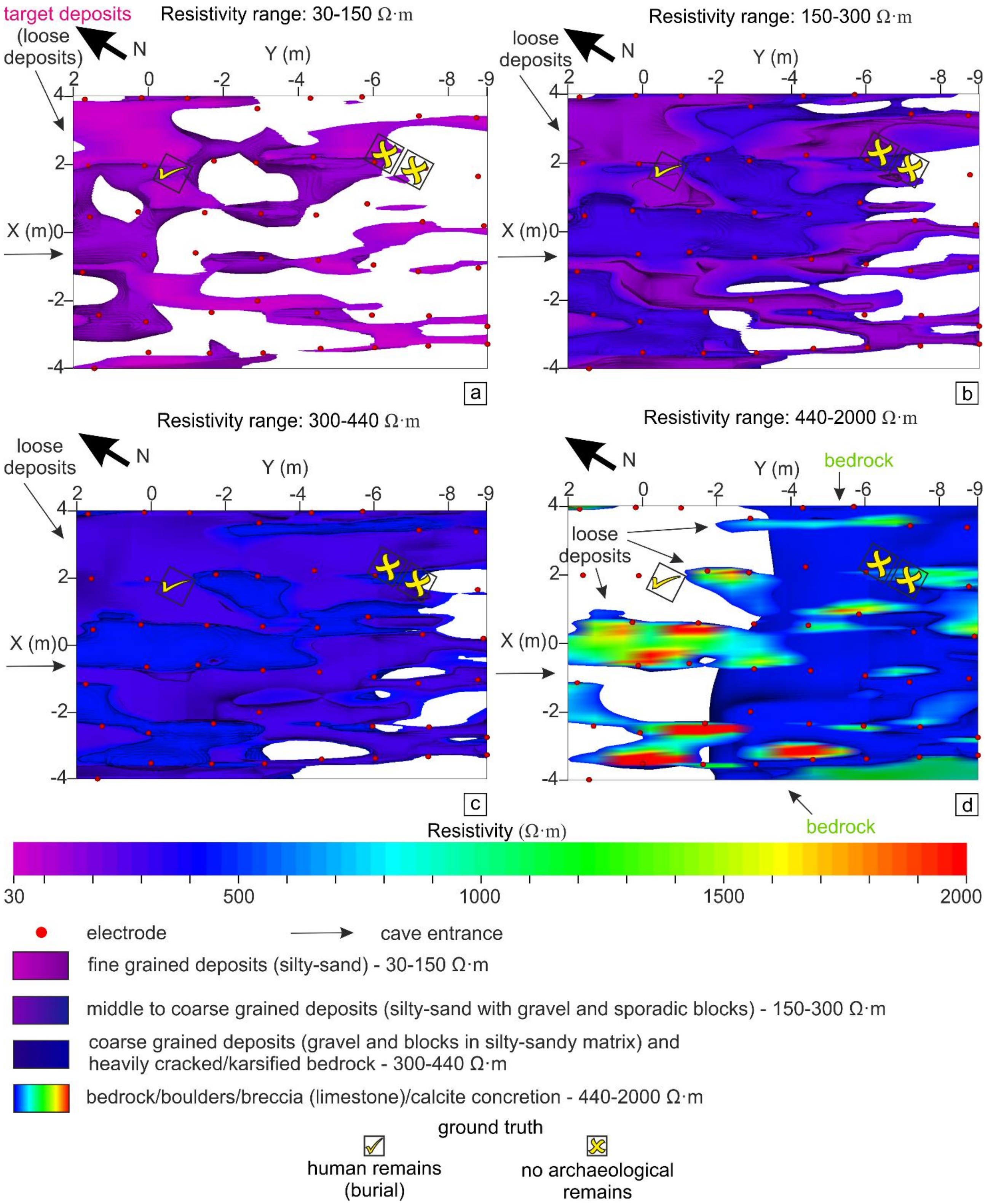

Fig. 5: Plan view of different resistivity range extractions from the 3D inverse resistivity model along with lithological description.

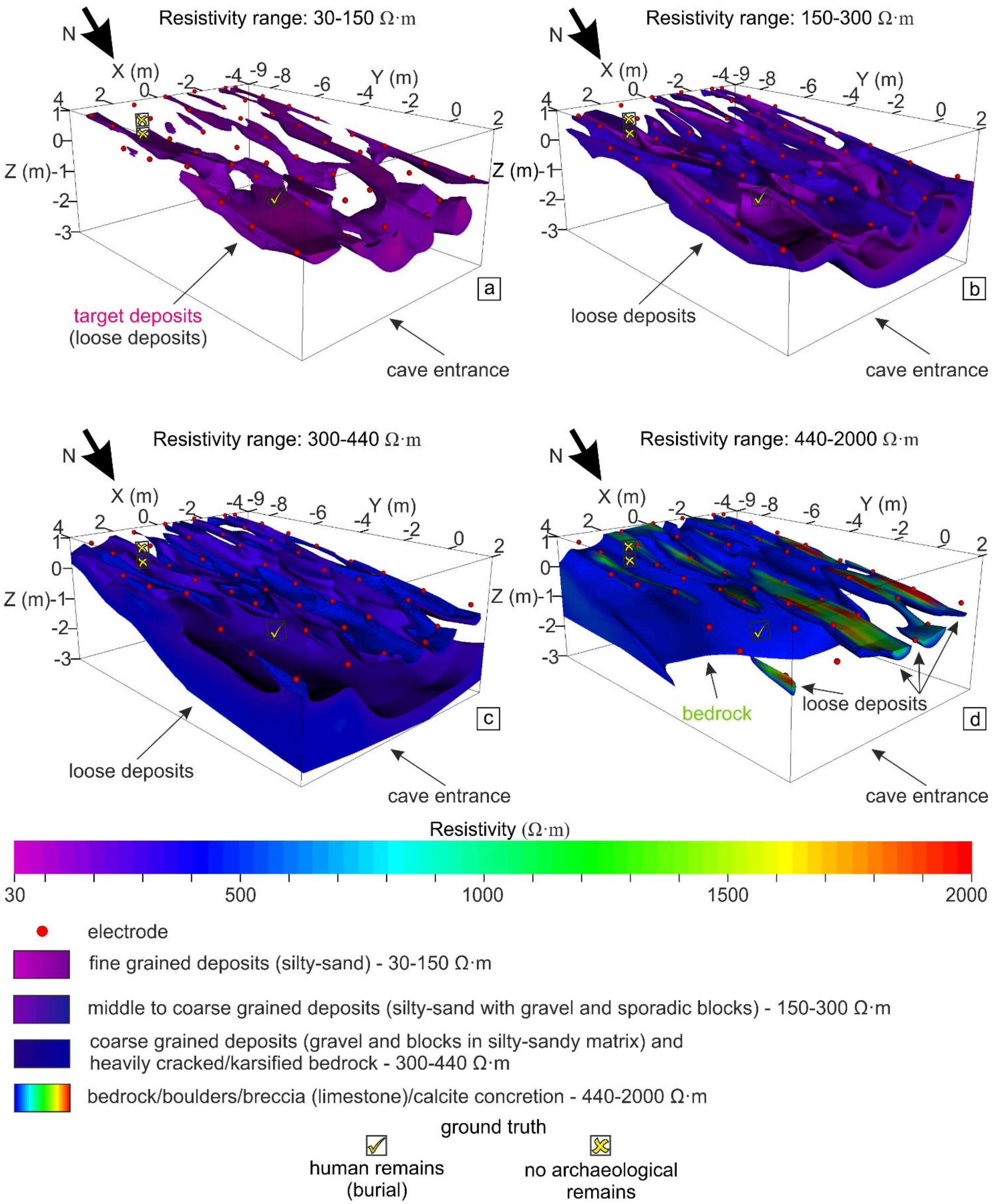

Fig. 6: Perspective view from above of different resistivity range extractions from the 3D inverse resistivity model along with lithological description.

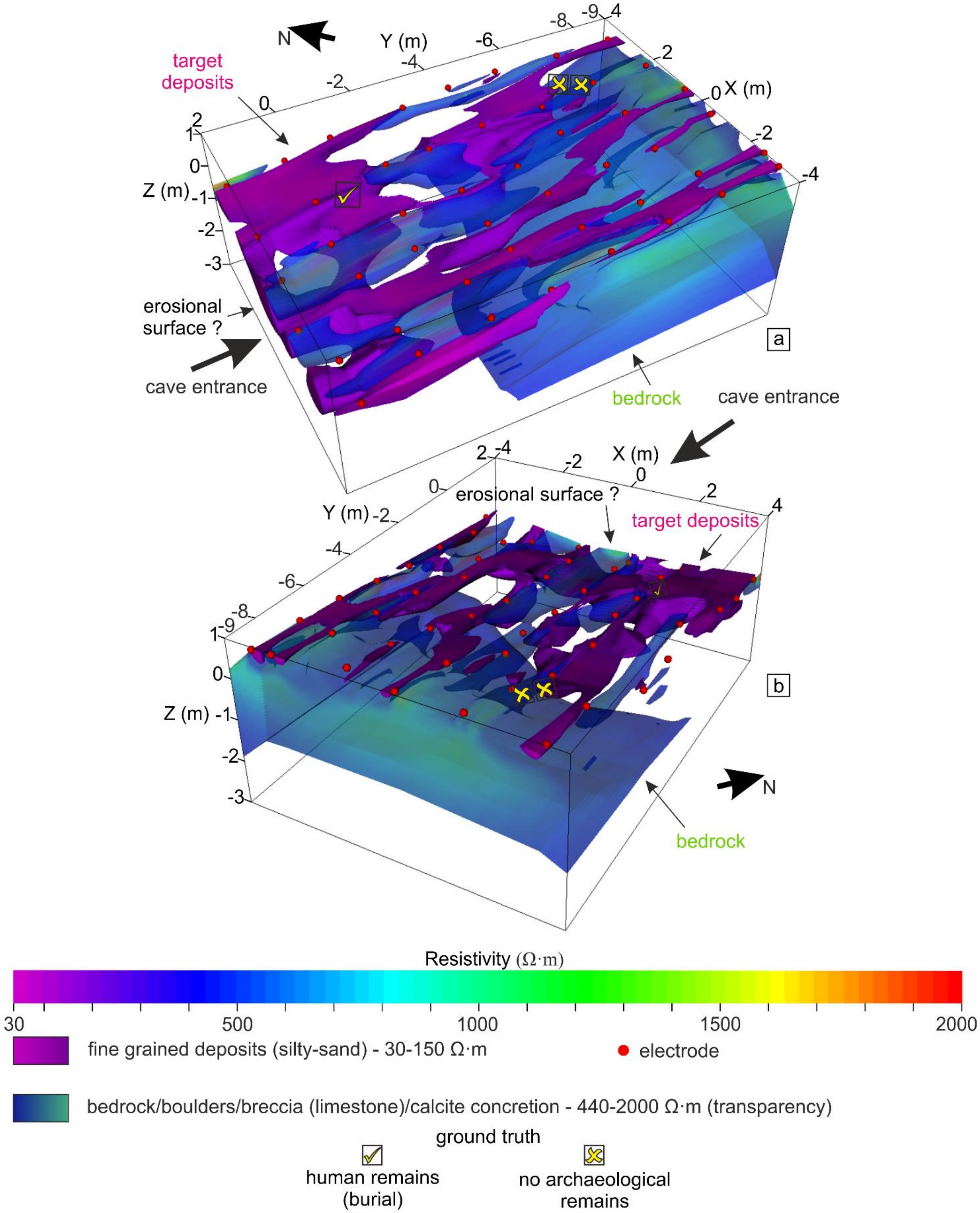

Fig. 7: Perspective views from above of different resistivity range extractions from the 3D inverse resistivity model: the low-resistivity unit (the most promising from an archaeological point of view) highlighted in opaque plot and the high-resistivity unit shown in transparent plot.

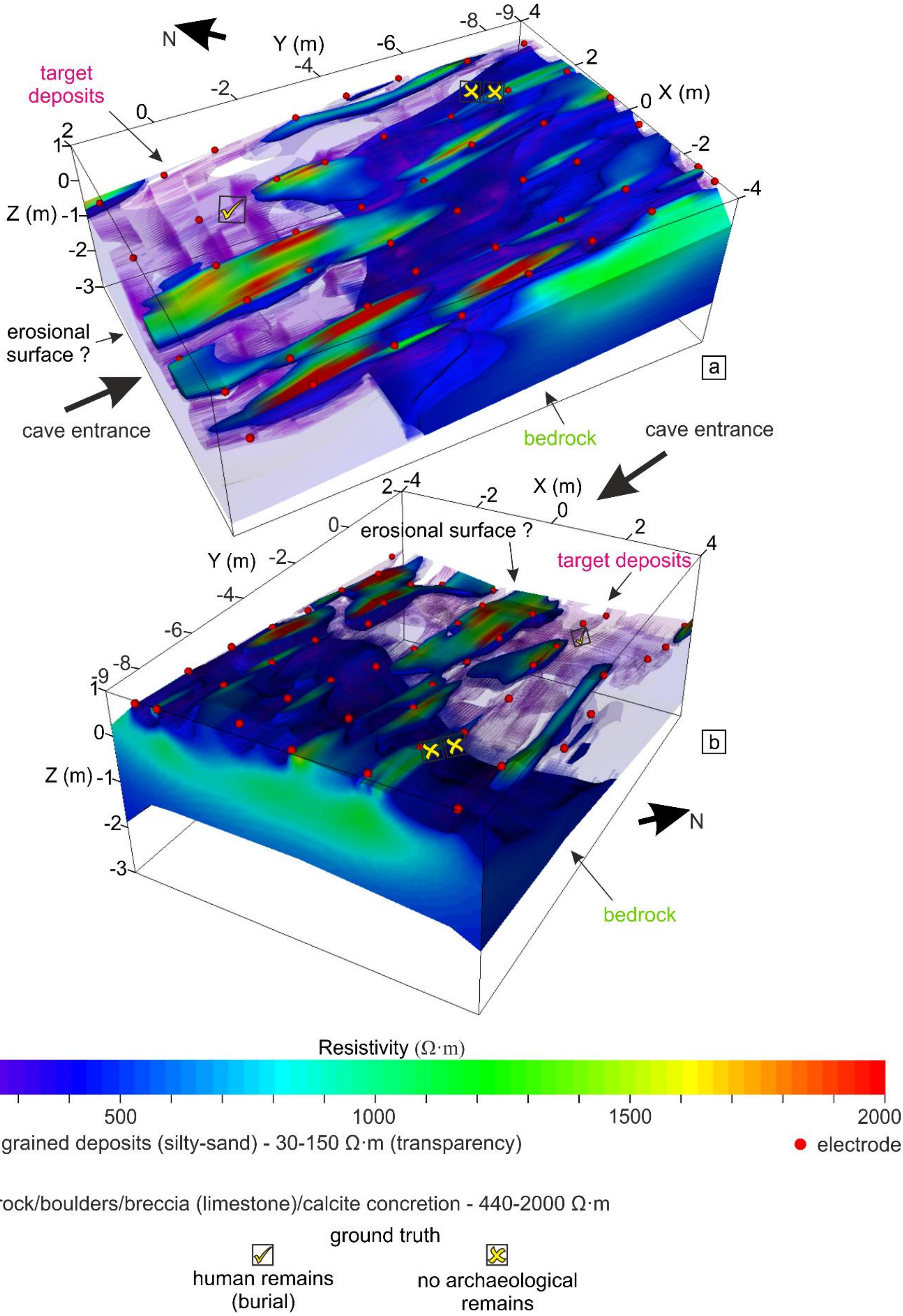

Fig. 8: Perspective views from above of different resistivity range extractions from the 3D inverse resistivity model: the high-resistivity unit highlighted in opaque plot and the low-resistivity unit (the most promising from an archaeological point of view) shown in transparent plot.

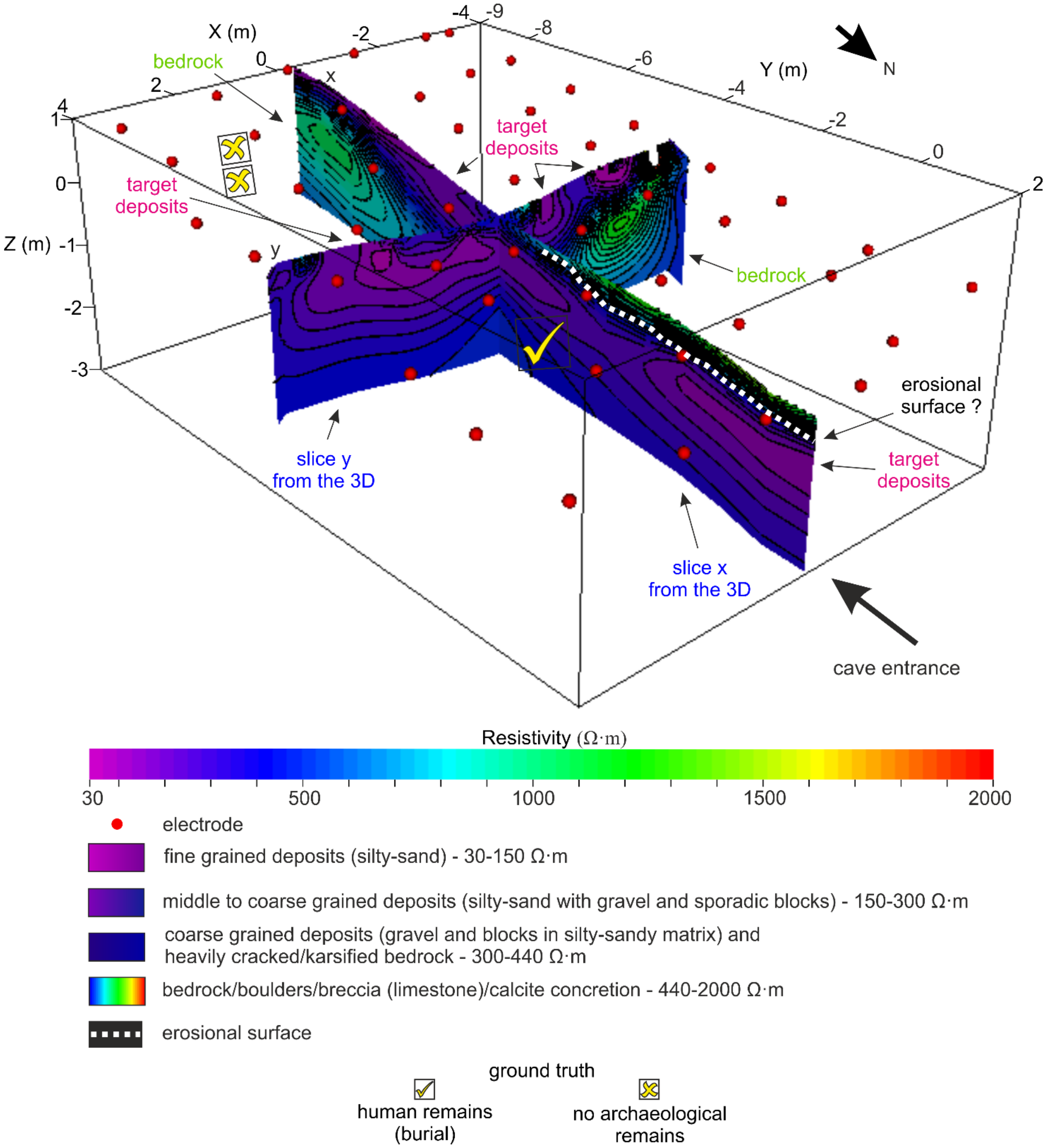

Fig. 9: Perspective view of X and Y plane slices extracted from the 3D inverse resistivity model showing the resistivity pattern along with lithological description.

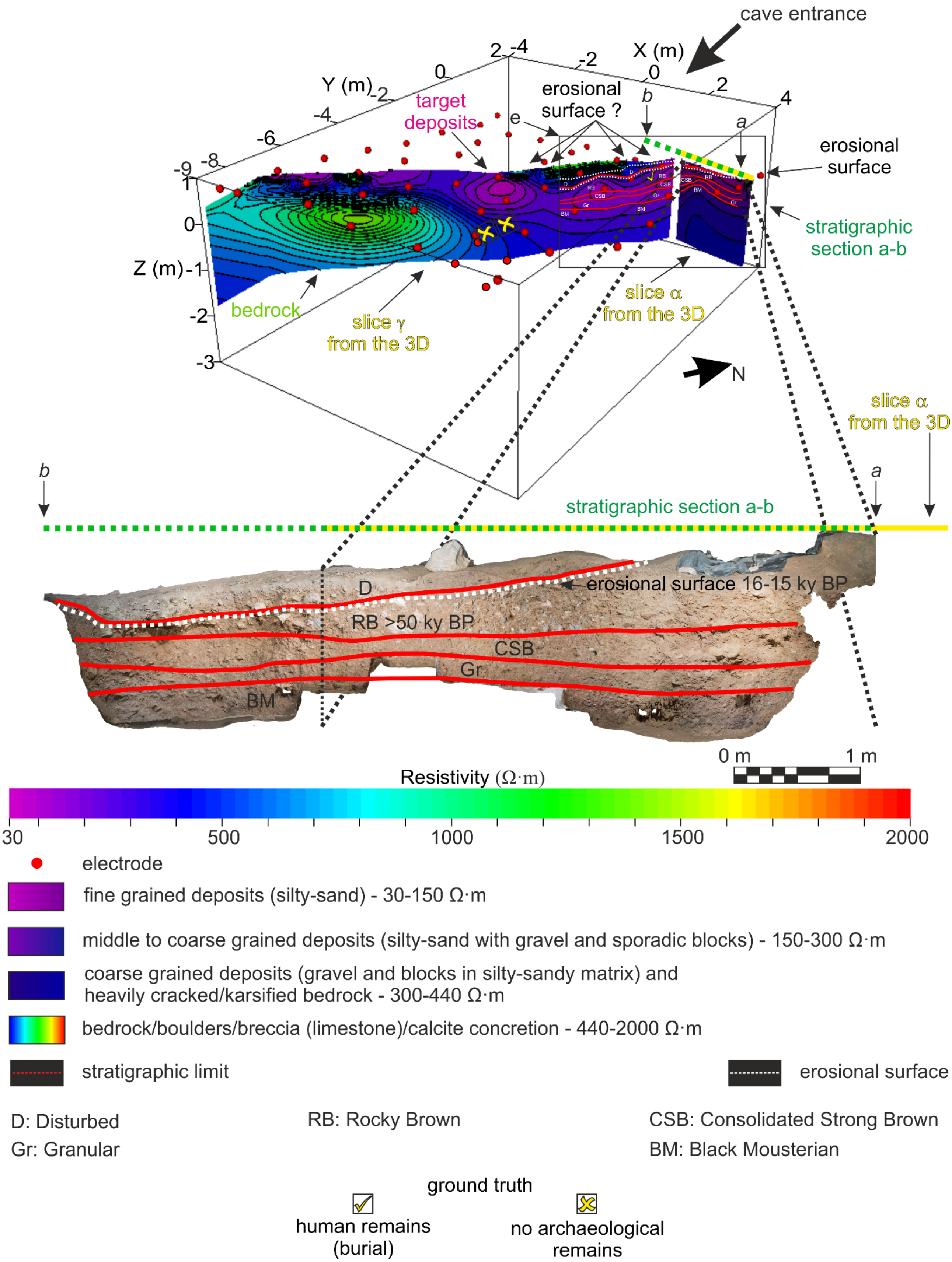

Fig. 10: Perspective view of α and γ plane slices extracted from the 3D inverse resistivity model along with the stratigraphic section a-b (main trench): the limits of the stratigraphic aggregates were

plotted on slice α which lies on the same plane as the stratigraphic sections a-b, to verify any correlation with the resistivity pattern and extrapolate the stratigraphic limits on slice γ.

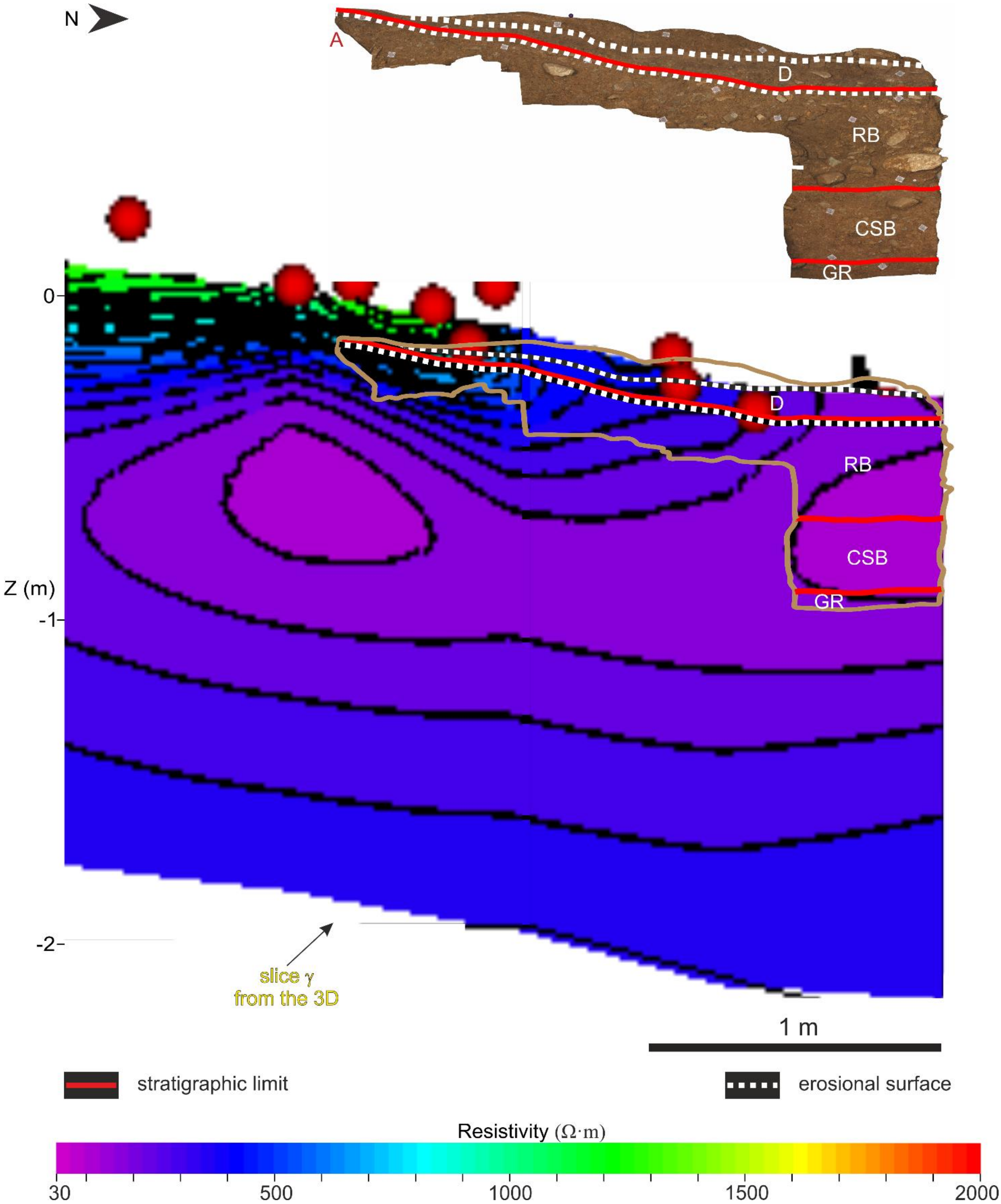

Fig. 11: Portion of the γ plane slice extracted from the 3D inverse resistivity model along with photograph and stratigraphic drawing of a portion of N-S profile: the limits of the stratigraphic aggregates were plotted on slice γ to verify any correlation with the resistivity pattern.

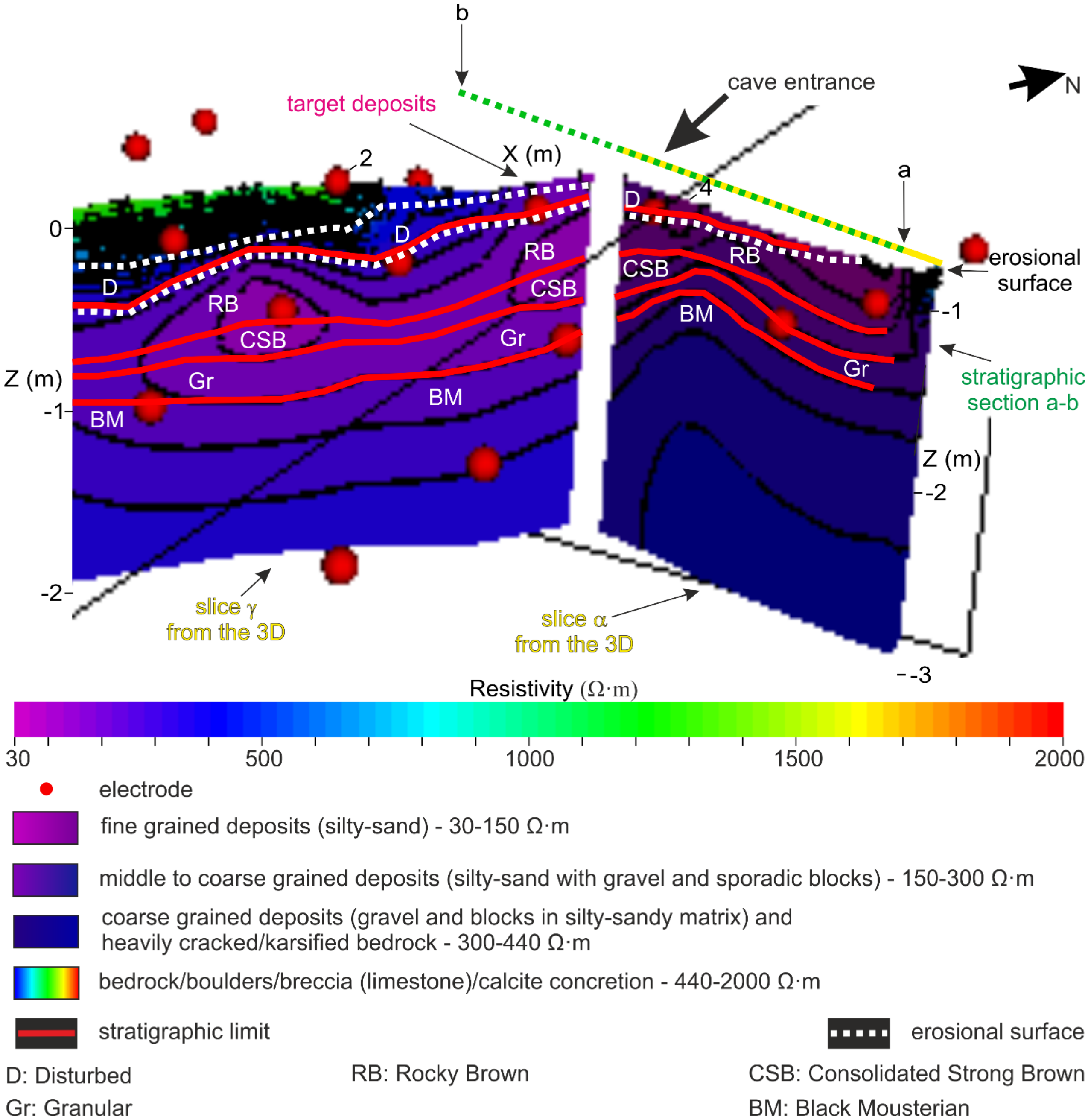

Fig. 12: Enlargement of the e portion of Fig 10: perspective view of α and (partly) γ plane slices extracted from the 3D inverse resistivity model along with stratigraphic limits derived from the stratigraphic sections a-b (main trench): the limits between the stratigraphic aggregates were plotted on slice α, which lies on the same plane as the stratigraphic sections a-b, to verify any correlation with the resistivity pattern and extrapolate the stratigraphic limits on slice γ.

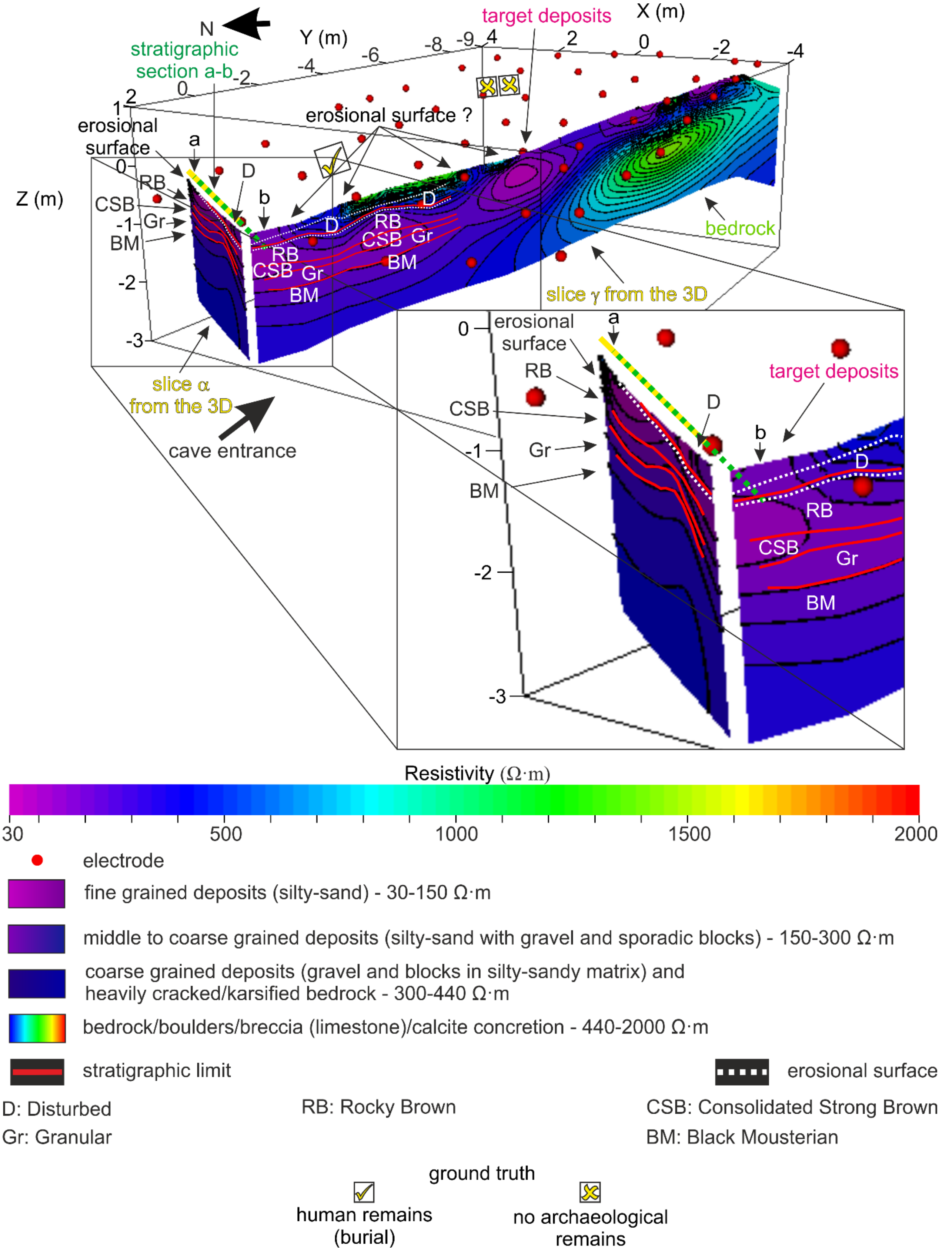

Fig. 13: Perspective view of α and γ plane slices extracted from the 3D inverse resistivity model along with the stratigraphic section a-b (main trench): the limits of the stratigraphic aggregates were

plotted on slice α which lies on the same plane as the stratigraphic section a-b, to verify any correlation with the resistivity pattern and extrapolate the stratigraphic limits on slice γ.

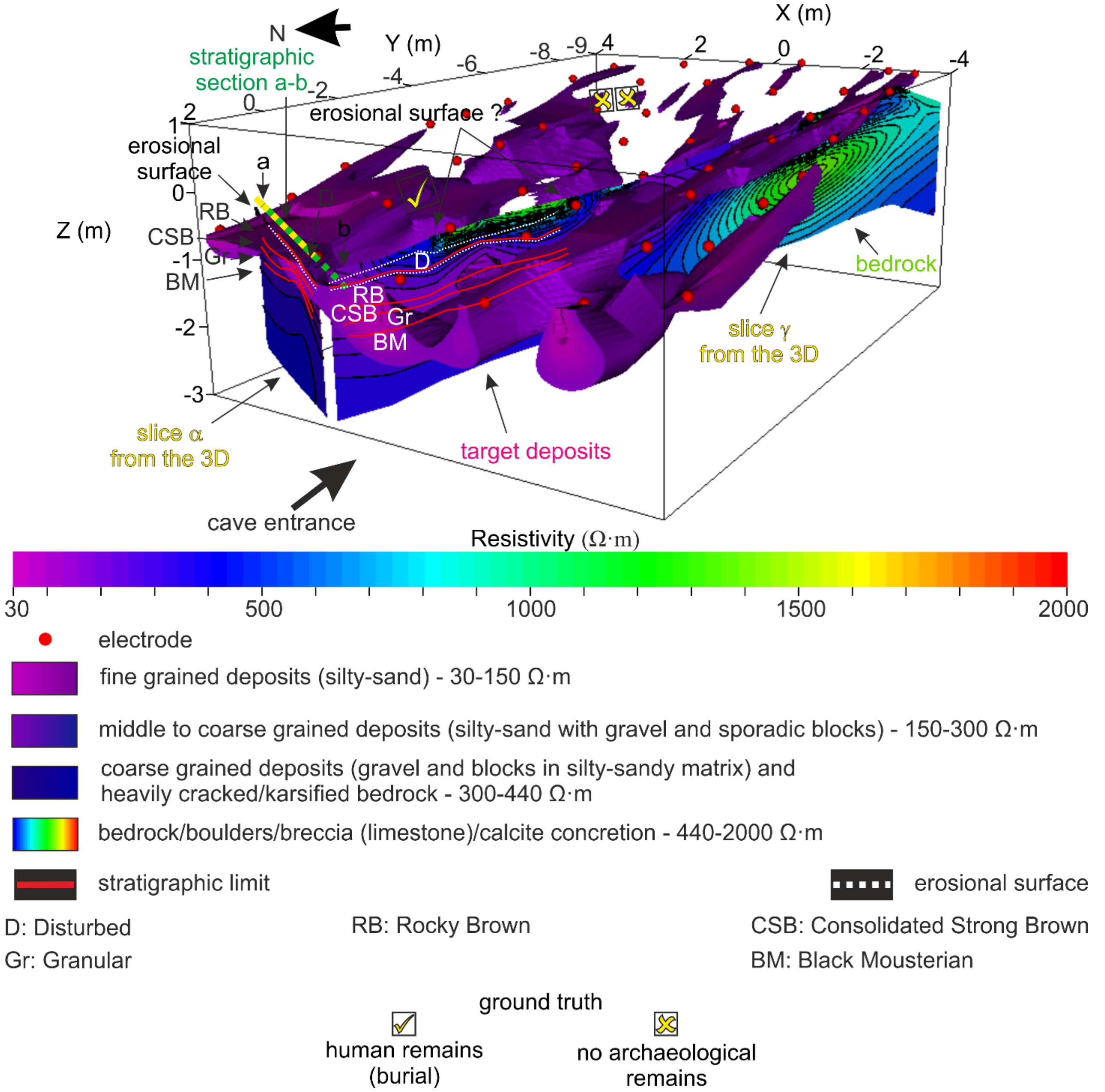

Fig. 14: Perspective view of α and γ plane slices extracted from the 3D inverse resistivity model along with the stratigraphic section a-b (main trench): the limits of the stratigraphic aggregates were plotted on slice α which lies on the same plane as the stratigraphic section a-b, to verify any correlation with the resistivity pattern and extrapolate the stratigraphic limits on slice γ; the 3D distribution of the low-resistivity unit, the most promising from an archaeological point of view has been also plotted for comparison.

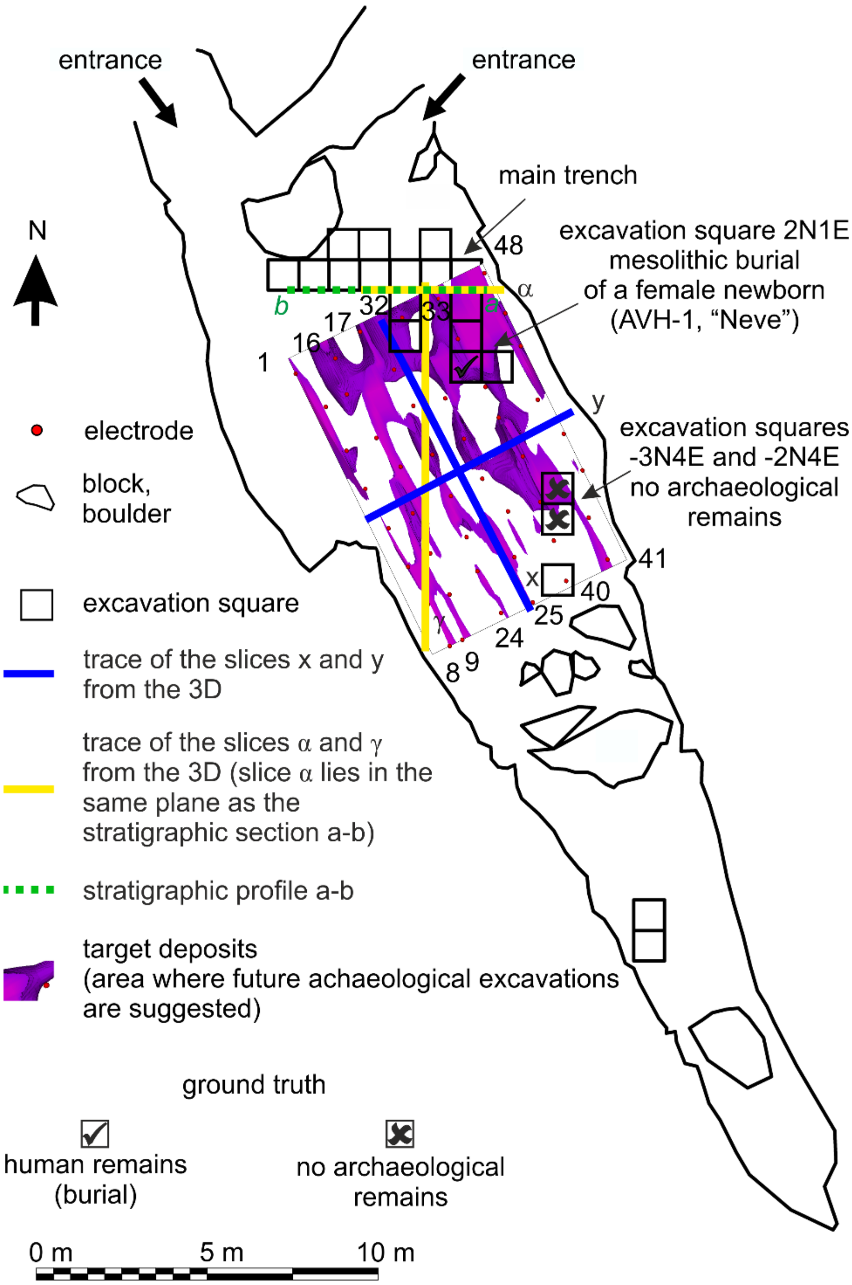

Fig. 15: Plan distribution of the low-resistivity unit (30-150 Ω·m, fine-grained deposits), the most promising from an archaeological point of view, along with the experimental layout of the ERT survey.

	Bulk electrical resistivity of the deposit/rock (Ω·m)	Bulk electrical conductivity of the deposit/rock, C_t (S/m)	Tortuosity factor, a	Cementation exponent of the deposit/rock, m	Bulk total porosity, ∅
Low-resistivity unit (L)	30 to 150	3.3333e-2 to 6.6667e-3	0.5 to 0.7	1.3	0.44 to 0.16
Middle-low resistivity unit (ML)	150 to 300	6.6667e-3 to 3.3333e-3	0.7 to 1	1.3	0.16 to 0.13
Middle-high resistivity unit (MH)	300 to 440	3.3333e-3 to 2.5e-3	1	1.3	0.13 to 0.1
High resistivity unit (H)	440 to 2.000	2.5e-3 to 5e-4	1	1.3 to 2	0.1

Table 1: Bulk total porosity estimation ∅ for the different resistivity units derived from the empirical relationship proposed by Archie (1942), along with the quantities involved in the estimation. The estimate involved the following values: electrical conductivity of the fluid C_w = 0,1 S/m, fluid saturation S_w = 0.7, saturation exponent n = 2.

Supplementary material

Text S1: Excavation, laboratory methods and documentation

Geological data on the StratAggs presented in this paper was collected in the field through standardized description of exposed profiles and in the laboratory using soil micromorphology. Field descriptions focused on defining stratigraphic units based on the morphology, extent and nature of stratigraphic contacts and definition of key lithological characteristics defining the stratigraphic units. In the field we characterized the grain-size, angularity and fabric of large blocks of roof spall. For finer grained sediments we emphasized frequency of grain-sizes using field texturing techniques to identify the proportion of clay, silt and sand. Color was determined using a Munsell soil chart. The presence of bedding or soil structures were also noted. Field observations were cross-checked using soil micromorphology, which is the study of intact blocks of sediment under the microscope. The blocks were wrapped in plaster and extracted directly from the excavated sediment profile, and loose soil samples. The blocks were hardened with a polyester resin and thin sectioned into 3 x 5 cm slides. The thin sections were examined using the naked eye and petrographic microscopes under plane-polarized light (PPL), cross-polarized light (XPL), oblique incident light (OIL), and blue-light fluorescence at magnifications ranging from 20-200x, following descriptive and analytical guidelines established by Bullock et al. (1985), Courty et al. (1989), and Stoops (2003). We were able to determine the composition of sedimentary components and the spatial and stratigraphic relationship between aggregates using petrographic analyses of thin sections. Grain-size classification followed the Wentworth scale.

References

Courty, M. A., Goldberg, P., Macphail, R., Soils and micromorphology in archaeology. (Cambridge University Press, Cambridge, 1989).

Stoops, G., Guidelines for analysis and description of soil and regolith thin sections. (Soil Science Society of America, Madison, 2003).

Bullock, P., Fedoroff, N., Jongerius, A., Stoops, G., Tursina, T., 1985. Handbook for Soil Thin Section Description. Waine Research Publications, Wolverhampton, UK.

Combined array	**Number of measures**	**Minimum resistivity (ohm·m)**	**Maximum resistivity (ohm·m)**	**Average resistivity (ohm·m)**	**Standard deviation (ohm·m)**
DD+W+WS)	432	46	1265	289	0

Table S1: Quality of resistivity raw data

Iteration	Number of measures	Chi-squared error	RMR error (ohm·m)
1	432	62481	36.1
2	432	5133	10.3
3	432	330	2.6

Table S2: Misfit of inverted resistivity data

Clayey silt with minor sand and gravel components with a dark greyish brown color.

Clayey silt with fine sand and gravel with a dark yellowish brown color. It displays a weakly developed subangular blocks structure.

Clayey silt with fine sand and gravel with a dark yellowish brown color. It appears more compact and displays a massive structure.

Medium sandy silt with granules and gravel with a brown to dark yellowish brown color. It exhibits a coarse crumb structure.

Silty-sand with medium to small altered gravel with a dark greyish brown color.

Fig. S1: Photographs from main trench (stratigraphic section a-b, E-W profile, Fig. 2), lithological description of the aggregates and associated images.